Article

Light-Emitting Electrochemical Cells of Single Crystal Hybrid Halide Perovskite with Vertically Aligned Carbon Nanotubes Contacts

Pavao Andričević,[†] Xavier Mettan,[†] Márton Kollár,[†] Bálint Náfrádi,[†] Andrzej Sienkiewicz,[†,‡] Tonko Garma,[§] Lidia Rossi,[†] László Forró,*[,†] and Endre Horváth*[,†]

[†]Laboratory of Physics of Complex Matter (LPMC), Ecole Polytechnique Fédérale de Lausanne, Centre Est, Station 3, CH-1015 Lausanne, Switzerland

[‡]ADSresonances SARL, Route de Genève 60B, CH-1028 Préverenges, Switzerland

[§]Power Engineering Department, Faculty of Electrical Engineering, Mechanical Engineering and Naval Architecture, University of Split, Split, Croatia

Ⓢ Supporting Information

ABSTRACT: Based on the reported ion migration under an electric field in hybrid lead halide perovskites we have developed a bright, light-emitting electrochemical cell with $CH_3NH_3PbBr_3$ single crystals directly grown on vertically aligned carbon nanotube forests as contact electrodes. Under the applied electric field, charged ions in the crystal drift and accumulate in the vicinity of the electrodes, resulting in an *in operando* formed p−i−n heterojunction. The decreased interface energy barrier and the strong charge injection due to the CNT tip enhanced electric field result in a bright green light emission up to 1800 cd/m^2 at room temperature (average ≈ 60 cd/m^2). Beyond the light emission, this original device architecture points to the possibility of implementing vertically aligned CNTs as electrodes in operationally stable perovskite-based optoelectronic devices.

KEYWORDS: Perovskite light emission, room temperature, switchable photovoltaic effect, light-emitting electrochemical cells, vertically aligned carbon nanotubes
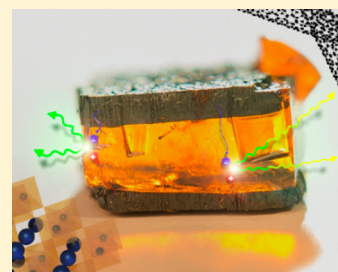
In the past decade semiconducting organic−inorganic lead halide perovskites, such as methylammonium lead triiodide, $CH_3NH_3PbI_3$ (MAPbI$_3$), and methylammonium lead tribromide $CH_3NH_3PbBr_3$ (MAPbBr$_3$), seem to become one of the most potent game-changers in the photovoltaic industry.[1−4] Most recently, apart from their use in next generation solar cells,[5] fast photon detection, even at low illumination intensities,[6] gas sensing,[7] promising thermoelectric figure of merit,[8,9] memristive effects,[10] optically switched ferromagnetic behavior in magnetic ions doped MAPbI$_3$ single crystals has also been demonstrated.[11]

For solar cells the detailed balance equation requires external luminescence efficiency close to 100% to attain the Shockley−Queisser limit of ≈33.5%, thus, implying that an excellent solar cell material must also be an excellent light emitter. As a result, perovskites have rapidly transitioned from breakthrough materials for solar cells to exceptional semiconducting materials with wide-range of applications in light emission.[12] High photoluminescence combined with compositional flexibility place perovskites as robust technological candidates distinguished by their high color purity (fwhm ≈ 20 nm),[12] bandgap tunability to cover the entire spectrum of visible light,[13,14] and low-to-moderate ionization energy (IE) to form stable functional interfaces.[15]

Therefore, lead halide perovskites were successfully integrated into light-emitting optoelectronic prototype devices. Tunable amplified spontaneous emission and lasers,[16,17] light-

emitting field effect transistors,[18] and light-emitting diodes (LEDs) from the infrared[19] to bright-green range have been demonstrated.[20] A typical state-of-the-art perovskite LED possesses a complex, multilayer device architecture, which usually consist of: a hole-transport layer, a light-emitting sheet of 3D layered[19,20] or nanostructured[21,22] perovskite, an electron-transport layer and electrical contacts. The use of electron- and hole-transport layers is considered to be crucial for perovskite LEDs because it lowers the electron/hole injection energy barriers, resulting in low operation voltage and high electroluminescence (EL) efficiency.[23] However, fabrication of such devices is more complicated and necessitates utilization of orthogonal solvents and air-sensitive transport layers. Finding alternative material for electrodes is therefore essential for commercial applications of perovskite-based optoelectronic devices.

Here we present a fairly simple architecture for light-emitting device, which consists only of two components, methylammonium lead tribromide (hereafter, MAPbBr$_3$) and vertically aligned carbon nanotube (VACNT) forests as contact electrodes. The operational principle is based on ion migration under an electric field. The space charge at the contacts reduces the barrier for charge injection, and the electrons and holes recombine in the crystal, resulting in light
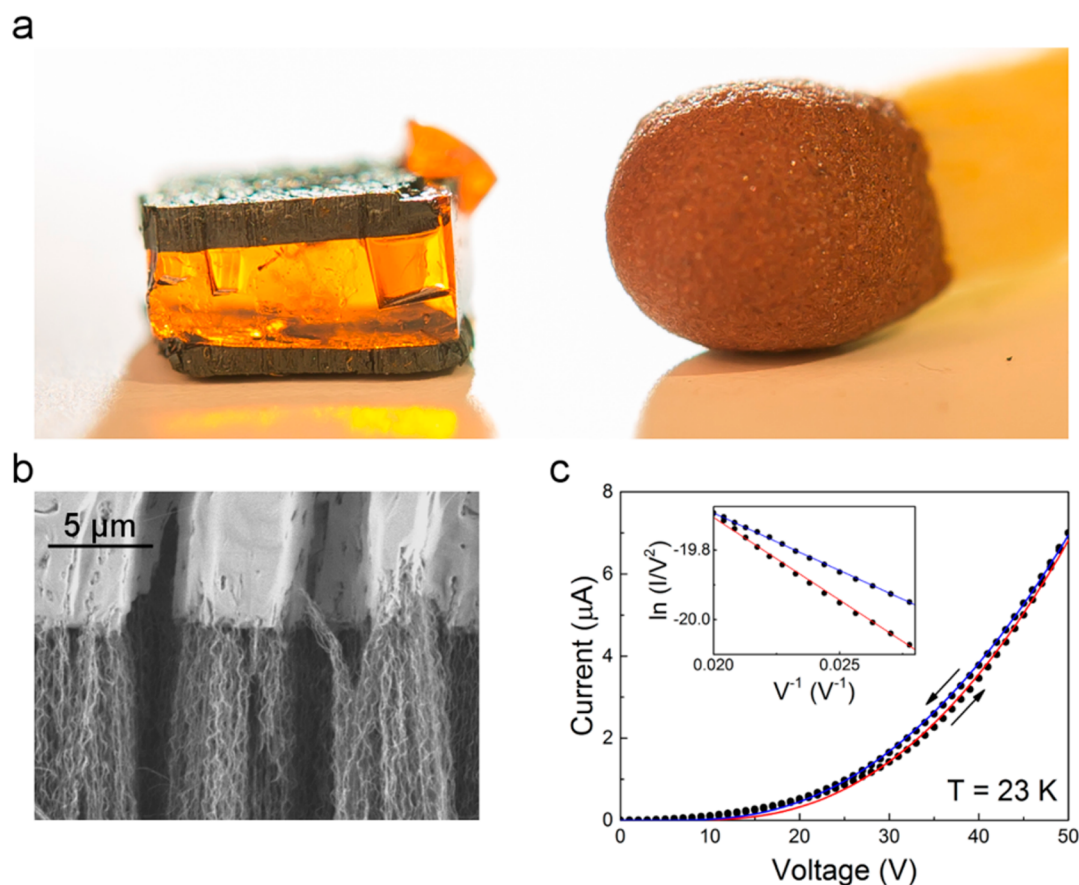
Figure 1. Presentation of the light-emitting electrochemical cell: (a) Optical image of a MAPbBr$_3$ single crystal sandwiched between two VACNT electrodes, resulting in a symmetric architecture (the match gives the scale); (b) SEM image of the interface between MAPbBr$_3$ and the engulfed VACNT electrodes; (c) Current−voltage characteristics of a symmetric device. The inset shows an essential feature of the device: the very efficient charge injection from CNTs by field emission represented by the Fowler-Nordheim plot.

emission. We take advantage of the strong electric field enhancement at the nanotubes tip for increased charge injection (up to 3 mA) into the crystal. The basic principle of our device is very similar to the mechanism of light-emitting electrochemical cells (LECs).[24−29] These light-emitting devices are often very complex, employing a broad range of active ion-conducting layers—from varius types of polymer to, more recently, perovskite/ionic electrolyte composites. In this context, the simple single crystal-based device described herein presents an unprecedented color purity for an LEC (full width at half-maximum of 7 ± 1 nm at 20 K), and the operation extends to room temperature, achieving an average brightness of ≈60 cd/m^2 (50 μA) up to flashes of maximum brightness of 1800 cd/m^2 at 2.8 mA. Knowing the ease for growing both MAPbBr$_3$ and VACNT, this result represents a viable route for future light-emitting devices, as well expanding the family of hybrid perovskite LECs.

RESULTS AND DISCUSSION

Perovskite light-emitting devices were fabricated by immersing VACNT forests into a saturated solution of MAPbBr$_3$. Under the inverse temperature crystal growth conditions,[30] the fast-growing single crystal gradually protruded and engulfed the individual carbon nanotubes (CNTs). Elemental analysis by EDX in Figure S1 shows clearly the interfaces and the engulfed, overlapping region between CNTs and MAPbBr$_3$, resulting in a three-dimensionally enlarged MAPbBr$_3$/VACNT

junction.[31] Such process, repeated on the opposite side of the perovskite single crystal, allow vertically aligned CNTs to latch also onto this facet, thus forming a symmetric device architecture, with double VACNT electrodes (Figure 1a,b). This is our central device (most of the discussion is addressed to it), but for the sake of comparison, an asymmetric contact device was also prepared with one VACNT and one silver electrode.

An important feature of our device is field emission from VACNTs, since carbon nanotubes are well-known to act as field emitters in vacuum[32] or in a dielectric, in this case MAPbBr$_3$. Field emission is a charge-injection mechanism occurring when electrons tunnel through a potential barrier under a bias lower than the breakdown voltage. Experimentally, its signature is observed in the $I-V$ measurements, as provided by the empirical Fowler and Nordheim equation:[33] $I = AV^2 \exp(-B/V)$, where A and B depend on the geometry and local environment of the field-emitters and on the dimensions of the device. The linear relationship between $\ln(I/V^2)$ and $1/V$ in the inset of Figure 1c and in Figure S2 thus support field emission from VACNTs into MAPbBr$_3$, at low and ambient temperatures. Interestingly, the slope (the coefficient B) in the inset varies with the sweep direction, pointing toward a change of the geometry of the tunneling barrier.

The $I-V$ characteristics for both the symmetric and the asymmetric device architectures were collected under white light illumination. In our previous work it was shown that these
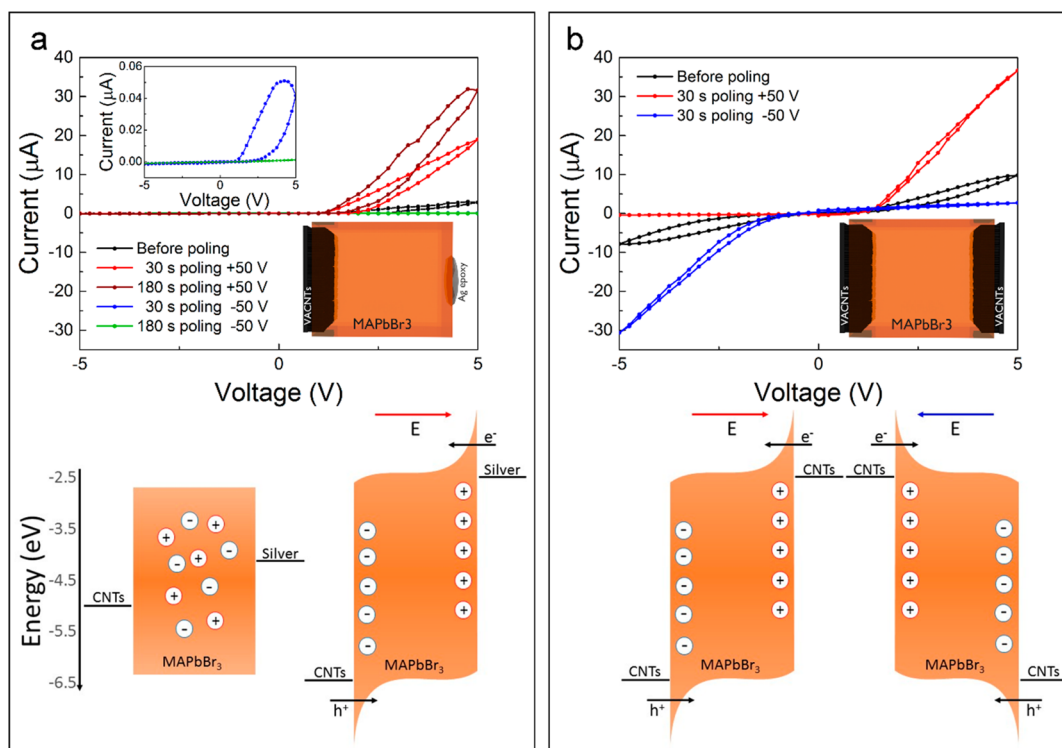
Figure 2. $I-V$ characteristics of the (a) asymmetric device (sketched in the inset) and (b) of the symmetric device (sketched in the inset). The schematic representation of the energy level of the contacts and the position of the ions in open circuit conditions and under an applied external electric field is given below the $I-V$ curves. They were collected under visible light illumination (intensity 1.02 mW cm^{-2}), before and after poling treatment, with applying different bias voltage polarities. The voltage was swept from 0 to ± 5 V and back. The current intensities through the device attain lower or higher values while increasing or decreasing bias voltage, respectively. Inset (a): Suppression of diode characteristics of the asymmetric device after reverse bias poling.

devices (asymmetric photodiodes) could serve as very sensitive light detectors, capable of detecting low light intensities down to nano-Watts.[31] One could notice that hysteresis is present in the $I-V$ characteristics and has been associated with the inertia of ion migration in forward and reversed biases.

The characterization is performed by $I-V$ measurements for both types of devices before and after performing voltage preconditioning, called poling, creating space charge regions.[10,34] As shown in Figure 2a,b, the $I-V$ characteristics acquired before poling treatment (black) were different for the two types of devices because of the differences in the work functions (Φ) of silver and CNTs. Silver has a Φ of 4.2 eV,[35] whereas that of CNTs is 5.05 eV.[36] Therefore, it is expected that the asymmetric Ag/MAPbBr$_3$/VACNT device (Figure 2a) has diode-like characteristics, allowing current to flow in the forward bias direction while suppressing the flow at reversed polarity due to the high Schottky barrier. After a constant bias voltage is applied for a short period of 30 s, the $I-V$ scans performed at rate of 2 V s^{-1} are different from those before poling. When the device is poled under forward bias, the diode characteristics are preserved, with an increase of current from 2 μA to 32 μA at 5 V (red). Interestingly, when a constant bias voltage of opposite polarity is applied, the diode characteristics are suppressed (blue) and even nullified (green) in the applied field range (from 2 μA falls to 2 nA at 5 V), obtaining symmetric $I-V$ characteristics after 180 s of poling (inset Figure 2a).

The modification of the $I-V$ characteristics is even more pronounced for the device with two VACNT electrodes (Figure 2b). Having symmetrical junctions, it has Schottky $I-$

V characteristics for both positive and negative bias voltages. However, if a constant bias voltage is applied for 30 s just before a quick voltage sweep (2 V s^{-1}), the $I-V$ characteristics completely change to a typical diode-like behavior. Now, current flows for voltages of the polarity of the previously applied bias. These changes as well as the time of relaxation back to the initial states depend on the time of voltage preconditioning and on the value of the bias voltage. The effects of poling in detail, as well as the changes of $I-V$ characteristic under different times of poling (10 s to 10 min) and poling voltages (1−200 V) are shown in Figure S3. Moreover, it is possible to change the polarity of the open circuit voltage, as seen in Figure S3e,f, achieving a switchable photovoltaic effect.[10]

In open-circuit conditions, ions of opposite signs are uniformly distributed within the active layer (Figure 2a). After a constant bias voltage is applied, the ions drift toward their respective electrodes and they accumulate at the perovskite/metal interface forming p−i−n heterojunction structures, increasing the injection rate of electrons and holes from the electrodes to the perovskite layer and governing the devices $I-V$ characteristics (Figure 2b). It is worth to mention that hysteresis was observed in perovskite solar cells, as well, attributing it to ion migration inside the perovskite layer.[37−40]

At bias voltages (V_b) larger than 5 V, the current through the device increased over 3 orders of magnitude (from nA to μA) before saturating. Remarkably, at ambient conditions and starting from the current intensities through the device of ~50 μA, a bright green EL was first observed for the asymmetric device (Figure S4a). Voltages much larger than the band gap

were used to achieve this critical current for light emission. Nevertheless, due to the large thickness of our single crystal devices (>1 mm), the external electric field was never larger than 200 V mm^{-1}.

To achieve light emission for both polarities, the focus had been moved to the symmetrical device architecture employing VACNTs as both electrodes on the perovskite single crystal. The device, previously conditioned to show diode-like behavior, exhibit light emission with further poling at room temperature in ambient conditions. For this device architecture, light emission is visible for both polarities, as shown on Figure S4b. Interestingly, the depletion region, which arises due to the high electric field ($\sim$10 V mm^{-1}), which is the region where the bright light emission is observed, is always near the interface with the lower potential, as was the case for the asymmetric device.

Bright green light is emitted at room temperature in the form of repetitive flashes of 100−120 Hz. In 20 s of acquiring light intensity and simultaneously measuring the current through the device, more than 40 excitations can be visible from multiple locations near the active surface of the device (Figure 3a). This yields an average luminance of $\sim$60 cd/m^2 for current as low as 50 μA. At higher currents, more charges are injected into the single crystal, resulting in brighter (max. 1800 cd/m^2 for 2.8 mA current) and more frequent flashes (Figure 3b). Importantly, stable and continuous light emission has not been observed at ambient conditions. It is likely that the space charge created by the migrated ions in electric field is exposed to thermal fluctuations. The fluctuations change the barrier structure in time, resulting in a fluctuating injected current and light intensity. Current instability at a constant voltage has been common for MWCNT field emitters.[32] However, these emitters observe switching between discrete current levels at low currents, reaching more stable emission at higher currents, whereas the perovskite light-emitting device exhibits random fluctuations, increasing with the value of current. Nevertheless, this is still an open question and should be taken into further consideration.

These fluctuations are damped by cooling the system down to cryogenic temperatures, because the mobility of ions is strongly reduced. The intensity of the injected current became stable, producing a continuous light emission. For example, at 25 K a very bright light emission was observed as seen in the inset of Figure 3c. Luminance−current versus applied voltage (LIV) of the symmetric LEC device for both negative and positive voltages is shown in Figures 3c and S5, respectively. Since the light emission comes from the recombination of electrons and holes in the perovskite, it is expected that the EL intensity correlates with the injected current in MAPbBr$_3$. This is fully confirmed by the LIV measurements at 25 K as well as their dependence with temperature (Figure S5). Continuous light emission stopped at 100 K, but flashes of light with quick changes of intensities could be followed up to room temperature. The device showed stable light emission for up to 1 h operation (Figure S5f). The light emission at room temperature, in the form of flashes, and at low temperatures, as a constant light in the dependence of voltage, can be seen in the video in the Supporting Information.

The spectral analysis of the emitted light at 20 K was performed for turn-on voltages in the range of 100 to 200 V and −30 to −40 V. The different colors of the emitted light for the two cases are already visible with the naked eye (see inset to Figure 4). Two sets of spectra with similar intensity count
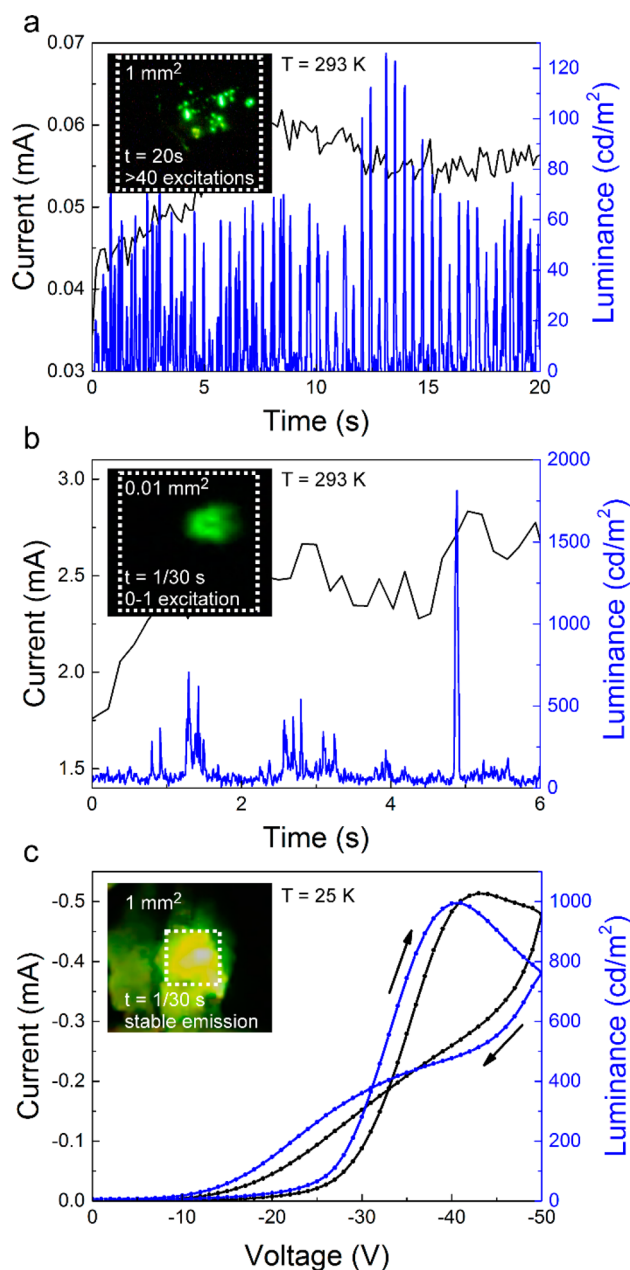

Figure 3. (a) Luminance−current in time for an applied bias voltage of 20 V at room temperature. Inset: Optical image of >40 flashes of light of light during 20 s at room temperature. (b) Luminance−current in time for an applied voltage of 40 V (>2 mA current) at room temperature. Inset: Screen shot of a video of the light emission at room temperature showing the emitting surface of less than 250 μm^2. (c) Luminance−current vs voltage at cryogenic temperatures (25 K). Inset: Screen shot of a video of the light emission showing stable light emission with an active emitting surface of 1 mm^2.

numbers were chosen of both polarities and fitted with a Gaussian function (Figure 4). One can read from these spectra two important information: (i) the redshift by 20 nm of the negative bias spectra compared to the spectra acquired for positive voltages; and (ii) the very narrow full width at half-maximum (fwhm), of the order of 8 nm, which represents a high spectral purity. This latter fact is certainly due to the high crystallinity of the sample. In polycrystalline sample or in polymer LECs the spectra are broader multiple times due to the inherent disorder.[41] When applying 150 V, bright green
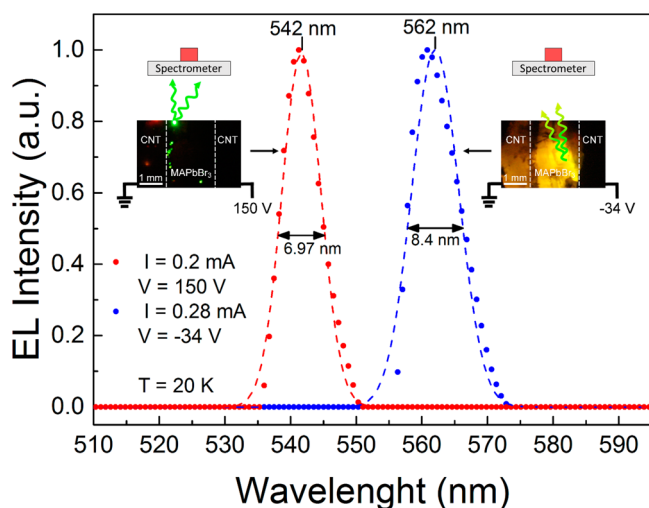
Figure 4. Typical normalized EL spectra recorded at 20 K in vacuum, at positive (red, +150 V) and negative (blue, −34 V) bias voltages, fitted with Gaussian function (dashed lines). Inset: Schematic illustration of the measurement setup with the photos of the light emission for the associated EL spectra.

spots with an emission peak centered at 542 nm wavelengths have the energy of the band gap. The −40 V biased case gives a red-shifted signal at 562 nm. It is likely that the different colors are due to different locations of recombination of the electron−hole pairs in the crystal. Our conjecture is that the green light is coming mostly from the crystal surface, while the yellowish light is from the bulk. Deep in the crystal, after recombination, the light is absorbed and re-emitted in cascades before reaching the spectrometer, and during this process, the slight energy loss results in a redshift of the spectra. On the other hand, for positive voltages, the recombination takes place near the surface, the light is directly emitted toward the spectrometer at a wavelength of 542 nm.[30] Similar arguments were put forward for red-shifted spectra in photoluminescence measurements by Wenger et al.[42] All the acquired EL spectra with their associated currents are given in Figure S6.

In order to obtain a more complete picture, about the limiting factors of the EL phenomenon in the symmetric architecture, light emission were collected with increasing temperatures from 23 to 40 K for the −40 V biased case (Figure 5a), and spectral analysis was performed (Figure 5b). At 23 K, two EL emission peaks were detected: one at 562 nm with a fwhm of about 7 nm, which is the same as in Figure 4, and a second broad peak at 590 nm with a fwhm of 10 nm. With increasing temperature, the intensity of the peak located at 562 nm weakens with no significant shift in wavelength and fwhm, while the peak centered at 590 nm increases in intensity, simultaneously undergoing a redshift and broadening, achieving a fwhm of 30 nm at 40 K (Figure 5c). We suspect that this peak emerges from radiative recombination at trap states in the perovskite single crystal. The increasing intensity with temperature corroborates with this attribution, as the population of these trap-states grows with temperature. With a further increase in temperature, higher absolute values of bias voltages and longer spectrometer integration times were needed to acquire spectra curves. This was possible only for the second peak at 590 nm up to 60 K, as shown in Figure S7. The redshift and the increasing fwhm is coming from the interaction of the created photons with lattice vibrations.

These features are confirmed on the asymmetric device recorded in the 40−300 K range shown in Figures S8 and S9.

In the above documented EL, the poling, which is the movement of ions under an electric field, is primordial (like in polymeric LECs), and the building up of the space charge layer near the contacts facilitate the charge injection into the crystal. To have a better insight into the time scale of this phenomenon, we have studied the time-dependence of the current increase upon applying a constant external voltage of 10 V during 10 h (Figure S10). The monotonic increase of current was fit by a triexponential function, giving three time constants. The shortest one (65 s) corresponds to the halogen ion movement, the intermediate (35 min) to the MA+ diffusion, and the longest one (7 h) to the slow thickening of the space charge layer. Such a hierarchy of the diffusion activation energies was found by Puscher et al.[43] as well. It has to be mentioned that no detectable degradation of the device was observed during the 10 working hours of operation at ambient atmosphere.

A further characterization of the device is done by measuring its capacitance (C) via the discharge current (similarly to Zhang et al.[44]) after poling of the VACNT/MAPbBr$_3$/VACNT sample (thickness 1 mm, surface area 10 mm^2). A certain bias (e.g., 2 V) was applied for a short period of time (≈15 s) in the dark to accumulate the ions at the perovskite/CNT interfaces, that is to charge the C_i, which represents the areal capacitance from the blocking of ions at the electrode interfaces.[38] The device was then rapidly switched to zero bias to measure the discharge current (Figure S11a, inset). The accumulated charge density is the time integral of the discharge current normalized to the perovskite electrode interface. From the measured charge densities of the accumulated ions at the interfaces under various biases (Figure S11a), one can extract a value of $C_i \approx 1$ μF cm^{-2}. This large areal capacitance exceeds that of conventional electrostatic capacitors,[45] with a typical value of 0.1 μF cm^{-2}. Furthermore, as shown in Figure S11b, the areal capacitance increases with the poling time. These results suggest that the organic−inorganic perovskites could serve as potential solid-state supercapacitors.

In general, the light-emitting electrochemical device are becoming increasingly popular and implement a broad range of active layers that possess the ionic conductivity.[24] Mostly, these are conjugated polymers, ionic transition-metal complexes, small molecules, and quantum dots, to recently used perovskite nanoparticles.[46] The latter one was used by Aygüler and co-workers, using MAPbBr$_3$ and FAPbBr$_3$ perovskites mixed with an ion polyelectrolyte (IP) to increase the ionic conductivity.[47] Following up this contribution, light emission was achieved in mixtures of perovskite nanoparticles with poly(ethylene oxide) (PEO) polymers,[41] composite films,[48] or as thin films using ITO/PEDOT:PSS and MoO$_3$/Au electrodes. For the sake of completeness, the best-in-class perovskite-based LECs and LEDs are shown in Table S2.

■ CONCLUSION

Here we demonstrated the operation of new, simple LECs based on MAPbBr$_3$ and VACNTs. Our VACNT/MAPbBr$_3$/VACNT device is the first room-temperature, single-crystal light emitter using symmetrical metallic electrodes without electrolyte or additional n- or p-type selective layers. Due to the single crystalline nature of the active material, the spectral purity of the emitted light is very high at low temperatures. The oriented carbon nanotubes by field emission inject a high
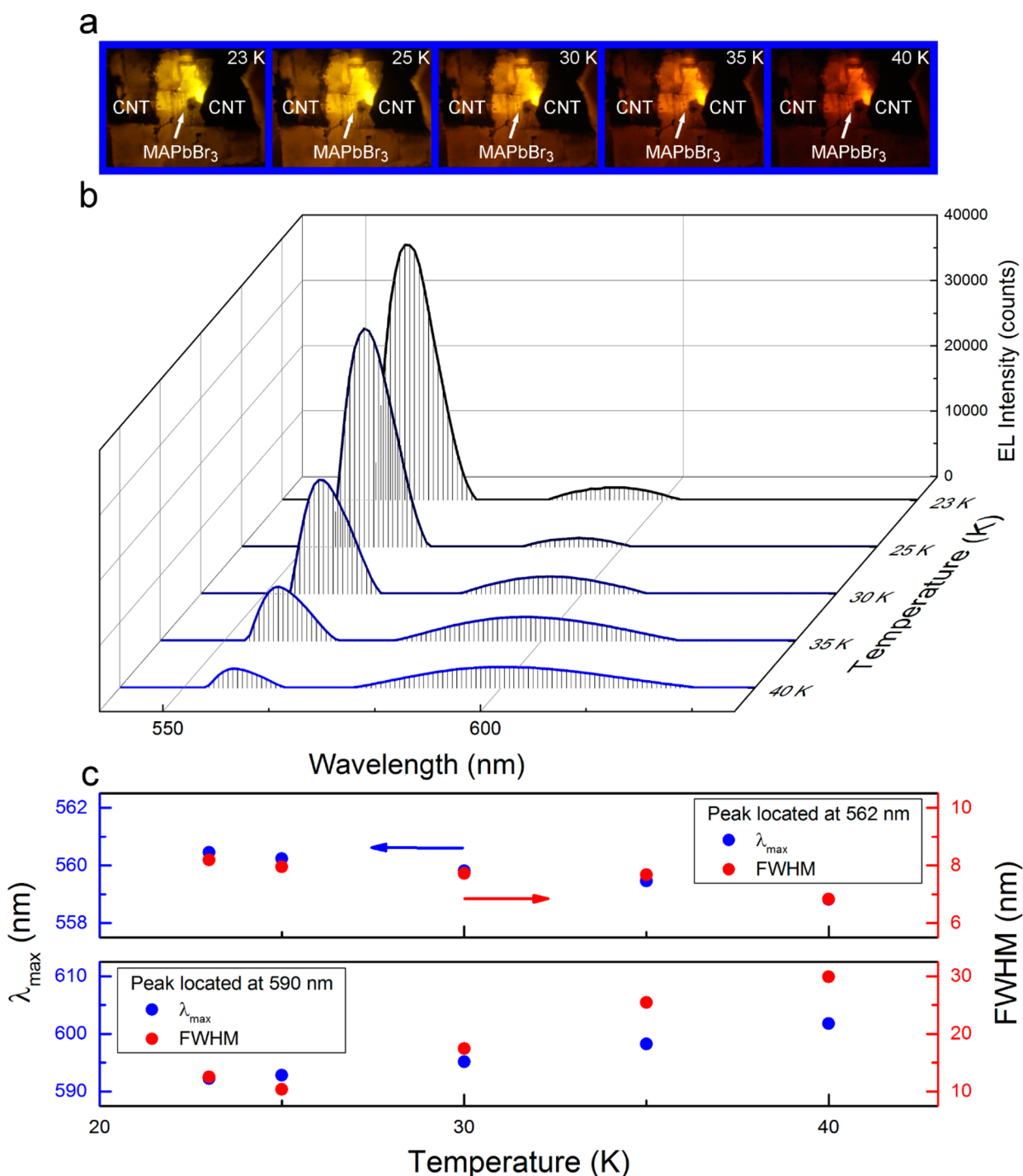
Figure 5. (a) Optical images of the light emission with −40 V of bias voltage as a function of temperature, highlighting the redshift. (b) Spectral analysis of the EL spectra reveal an emission peak at 562 and 592 nm at 23 K, which have different temperature dependences. (c) The temperature dependence of the wavelength and fwhm extracted from a Gaussian fit.

current density (due to the tip-enhanced electric field), which gives bright light emission up to 1800 cd/m^2, even at room temperature. The design developed herein points to the possibility of implementing vertically aligned CNTs as electrodes in operationally stable optoelectronic devices. The VACNT-based technology can also serve as a versatile platform for future electrode development.

■ EXPERIMENTAL SECTION

VACNT Growth. Carbon nanotubes were grown by catalytic chemical vapor deposition. First, transition metals, such as Fe, Co, Ni, or their alloys were used as the catalysts, while Al$_2$O$_3$, MgO, and SiO$_2$ as oxide supports. VACNT are then grown utilizing a special preparation protocol documented in our previous work[31,49,50] named the supergrowth method. The CNT self-assemble into vertically oriented cellular arrays during the growth on the substrate as high as 2.5 mm. The VACNT forest contain predominantly multiwall

CNTs and are 95% porous allowing the direct grow of perovskite SC on the VACNT forest.

Crystal Growth. Crystals of the methylammonium lead tribromide were synthesized by solution growth. The lead(II) acetate trihidrate (3.3 mmol, $Pb(ac)_2 \cdot 3H_2O$, >99.9%) was reacted with saturated HBr solution (6 mL, 48 wt % HBr in H_2O). The formed $PbBr_2$ precipitate is stable in the acidic solution. The respective amount (3.30 mmol) of methylamine (CH_3NH_2) solution (40 wt % in H_2O) was pipetted into the 5 °C ice cooled solution of $PbBr_2$. The cold solution avoids the evaporation of methylamine during the exothermic reaction. Orange colored microcrystallites of $CH_3NH_3PbBr_3$ were formed. The $MAPbBr_3$ crystals were recrystallized in a temperature gradient of 15 °C in the acidic media to get transparent, high purity crystals.

$MAPbBr_3$ single crystals were grown by inverse temperature crystallization from its saturated solution in DMF. $MAPbBr_3$ (0.8 g) was dissolved per cm^3 of DMF at room temperature. The substrate was immersed in the solution, and a $MAPbBr_3$ seed crystal was placed on the top of the VACNT. Crystal growth was initialized by increasing the temperature of the solution from room temperature to 40 °C with a heating rate of 5 °C per hour. We observed that the fast-growing seed single crystals gradually protruded and engulfed the individual nanotubes. These types of inclusions, when the original form of the included mineral is preserved in the host crystal is categorized as a protogenetic inclusion in mineralogy. The slow heating rate suppress the formation of new seed crystals in the supersaturated solution and our $MAPbBr_3$ seed crystal can grow rapidly on the substrate. When the required size of crystal was reached, the $MAPbBr_3$–VACNT composite was removed from the solution, wiped, and dried. The same growth method was repeated using the $MAPbBr_3$–VACNT junction as a seed crystal to obtain two VACNT electrodes on the perovskite single crystal.

Optoelectronic Characterization. All measurements of the I–V characteristics of the device and dependence to poling at room temperature were done in ambient conditions. The device characteristics have been determined by two-point resistivity measurements, using golden wires contacted with Dupont 4929 silver epoxy as electrical leads. A Keithley 2400 source meter allowed us to measure the current with <0.1 nA resolution while tuning the applied bias voltage, in the dark and under visible light illumination.

Intensity Measurements of the Light Emission at Room Temperature. A Thorlabs PM100D Compact Power and Energy Meter Console with its corresponding software were used to obtain the intensities of light with <0.1 nW resolution. The light-emitting device was contacted with two tungsten needles as electrical leads. A Keithley 2400 source meter was use to apply voltage to the sample and measure current with <0.1 nA resolution. The photodetector was positioned 1 cm from the sample at a small angle to simultaneously capture optical images or videos of the bright green light with a Canon EOS 600D camera (ISO1600). All measurements were done at room temperature and in an ambient atmosphere.

Intensity and Spectra Measurements of the Light Emission at Low Temperatures. To achieve stable light emission, the light device was mounted inside a close cycle cryostat with optical windows and brought to cryogenic temperatures (20 to 80 K) and high vacuum. A Keithley 2400 source meter was again used to apply voltage to the sample and

measure current with <0.1 nA resolution. The dependence of the light intensity with voltage and in time were determined by measuring the photocurrent of a Thorlabs FDS100 silicon photodiode, which was positioned ~5 cm from the sample behind an optical window. Likewise, the spectra of the emitted light were measured using an Ocean Optics QE65 Pro spectrometer. The light was collected using a series of lenses to an optical fiber, positioned on the cryostat optical windows. The spectra were acquired using the Ocean Optics SpectraSuite software. Care was taken to limit the current (max. 2 mA). With increasing temperatures, the absolute value of the voltage had to be adjusted (increased) in order to keep a sufficient current, required for light emission. Luminance of the device was calculated from the spectra at room and cryogenic temperatures, as shown in Figure S12. Due to many losses in our setup (optical windows, etc.) much lower values are obtained compared to direct measurements of intensities of the same device at room temperature. Optical images clearly show a much brighter light, so the intensities obtained by the silicon photodiode are calibrated as shown in the Supporting Information.

■ ASSOCIATED CONTENT

⊛ Supporting Information

The Supporting Information is available free of charge on the ACS Publications website at DOI: 10.1021/acsphotonics.8b01653.

> I–V characteristics of the light-emitting device under different pooling schemes, as well as room to cryogenic temperature characterization of the asymmetric LEC device (PDF)
>
> Video: The light emission at room temperature, in the form of flashes, and at low temperatures, as a constant light in the dependence of voltage (AVI)

■ AUTHOR INFORMATION

Corresponding Authors
*E-mail: laszlo.forro@epfl.ch.
*E-mail: endre.horvath@epfl.ch.
ORCID ⊙
Bálint Náfrádi: 0000-0001-9543-2970
Andrzej Sienkiewicz: 0000-0003-3527-7379
Endre Horváth: 0000-0001-7562-2267
Notes
The authors declare no competing financial interest.

■ ACKNOWLEDGMENTS

■ REFERENCES

(1) Lee, M. M.; Teuscher, J.; Miyasaka, T.; Murakami, T. N.; Snaith, H. J. Efficient hybrid solar cells based on meso-superstructured organometal halide perovskites. *Science* **2012**, *338*, 643−647.
(2) Kim, H.-S.; Lee, C.-R.; Im, J.-H.; Lee, K.-B.; Moehl, T.; Marchioro, A.; Moon, S.-J.; Humphry-Baker, R.; Yum, J.-H.; Moser, J. E.; et al. Lead Iodide Perovskite Sensitized All-Solid-State Submicron Thin Film Mesoscopic Solar Cell with Efficiency Exceeding 9%. *Sci. Rep.* **2012**, *2* (1), 591.

(3) Liu, M.; Johnston, M. B.; Snaith, H. J. Efficient Planar Heterojunction Perovskite Solar Cells by Vapour Deposition. *Nature* **2013**, *501* (7467), 395−398.

(4) Burschka, J.; Pellet, N.; Moon, S.-J.; Humphry-Baker, R.; Gao, P.; Nazeeruddin, M. K.; Grätzel, M. Sequential Deposition as a Route to High-Performance Perovskite-Sensitized Solar Cells. *Nature* **2013**, *499* (7458), 316−320.

(5) NREL Efficiency Chart. https://www.nrel.gov/pv/assets/pdfs/pv-efficiencies-07-17-2018.pdf (accessed November 14, 2018).

(6) Spina, M.; Lehmann, M.; Náfrádi, B.; Bernard, L.; Bonvin, E.; Gaál, R.; Magrez, A.; Forró, L.; Horváth, E. Microengineered CH$_3$NH$_3$PbI$_3$ Nanowire/Graphene Phototransistor for Low-Intensity Light Detection at Room Temperature. *Small* **2015**, *11* (37), 4824−4828.

(7) Bao, C.; Yang, J.; Zhu, W.; Zhou, X.; Gao, H.; Li, F.; Fu, G.; Yu, T.; Zou, Z. A Resistance Change Effect in Perovskite CH$_3$NH$_3$PbI$_3$ Films Induced by Ammonia. *Chem. Commun.* **2015**, *51* (84), 15426−15429.

(8) Mettan, X.; Pisoni, R.; Matus, P.; Pisoni, A.; Jacimovic, J.; Náfrádi, B.; Spina, M.; Pavuna, D.; Forró, L.; Horváth, E. Tuning of the Thermoelectric Figure of Merit of CH$_3$NH$_3$MI$_3$ (M = Pb,Sn) Photovoltaic Perovskites. *J. Phys. Chem. C* **2015**, *119* (21), 11506.

(9) Pisoni, A.; Jaćimović, J.; Barišić, O. S.; Spina, M.; Gaál, R.; Forró, L.; Horváth, E. Ultra-Low Thermal Conductivity in Organic−Inorganic Hybrid Perovskite CH$_3$NH$_3$PbI$_3$. *J. Phys. Chem. Lett.* **2014**, *5* (14), 2488−2492.

(10) Xiao, Z.; Yuan, Y.; Shao, Y.; Wang, Q.; Dong, Q.; Bi, C.; Sharma, P.; Gruverman, A.; Huang, J. Giant Switchable Photovoltaic Effect in Organometal Trihalide Perovskite Devices. *Nat. Mater.* **2015**, *14* (2), 193−198.

(11) Náfrádi, B.; Szirmai, P.; Spina, M.; Lee, H.; Yazyev, O. V.; Arakcheeva, A.; Chernyshov, D.; Gibert, M.; Forró, L.; Horváth, E. Optically Switched Magnetism in Photovoltaic Perovskite CH$_3$NH$_3$(Mn:Pb)I$_3$. *Nat. Commun.* **2016**, *7*, 13406.

(12) Veldhuis, S. A.; Boix, P. P.; Yantara, N.; Li, M.; Sum, T. C.; Mathews, N.; Mhaisalkar, S. G. Perovskite Materials for Light-Emitting Diodes and Lasers. *Adv. Mater.* **2016**, *28*, 6804−6834.

(13) Eperon, G. E.; Stranks, S. D.; Menelaou, C.; Johnston, M. B.; Herz, L. M.; Snaith, H. J. Supplementary Information Formamidinium of Formamidinium Lead Trihalide: A Broadly Tunable Perovskite for Efficient Planar Heterojunction Solar Cells. *Energy Environ. Sci.* **2014**, *7* (3), 982.

(14) Nedelcu, G.; Protesescu, L.; Yakunin, S.; Bodnarchuk, M. I.; Grotevent, M. J.; Kovalenko, M. V. Fast Anion-Exchange in Highly Luminescent Nanocrystals of Cesium Lead Halide Perovskites (CsPbX$_3$, X = Cl, Br, I). *Nano Lett.* **2015**, *15* (8), 5635−5640.

(15) Kulbak, M.; Cahen, D.; Hodes, G. How Important Is the Organic Part of Lead Halide Perovskite Photovoltaic Cells? Efficient CsPbBr$_3$ Cells. *J. Phys. Chem. Lett.* **2015**, *6* (13), 2452−2456.

(16) Xing, G.; Mathews, N.; Lim, S. S.; Yantara, N.; Liu, X.; Sabba, D.; Grätzel, M.; Mhaisalkar, S.; Sum, T. C. Low-Temperature Solution-Processed Wavelength-Tunable Perovskites for Lasing. *Nat. Mater.* **2014**, *13* (5), 476−480.

(17) Zhu, H.; Fu, Y.; Meng, F.; Wu, X.; Gong, Z.; Ding, Q.; Gustafsson, M. V.; Trinh, M. T.; Jin, S.; Zhu, X.-Y. Lead Halide Perovskite Nanowire Lasers with Low Lasing Thresholds and High Quality Factors. *Nat. Mater.* **2015**, *14* (6), 636−642.

(18) Chin, X. Y.; Cortecchia, D.; Yin, J.; Bruno, A.; Soci, C. Lead Iodide Perovskite Light-Emitting Field-Effect Transistor. *Nat. Commun.* **2015**, *6* (1), 8383.

(19) Jaramillo-Quintero, O. A.; Sánchez, R. S.; Rincón, M.; Mora-Sero, I. Bright Visible-Infrared Light Emitting Diodes Based on Hybrid Halide Perovskite with Spiro-OMeTAD as a Hole Injecting Layer. *J. Phys. Chem. Lett.* **2015**, *6* (10), 1883.

(20) Tan, Z.-K.; Moghaddam, R. S.; Lai, M. L.; Docampo, P.; Higler, R.; Deschler, F.; Price, M.; Sadhanala, A.; Pazos, L. M.; Credgington, D.; et al. Bright Light-Emitting Diodes Based on Organometal Halide Perovskite. *Nat. Nanotechnol.* **2014**, *9* (9), 687−692.

(21) Wong, A. B.; Lai, M.; Eaton, S. W.; Yu, Y.; Lin, E.; Dou, L.; Fu, A.; Yang, P. Growth and Anion Exchange Conversion of CH$_3$NH$_3$PbX$_3$ Nanorod Arrays for Light-Emitting Diodes. *Nano Lett.* **2015**, *15*, 5519−5524.

(22) Li, G.; Tan, Z. K.; Di, D.; Lai, M. L.; Jiang, L.; Lim, J. H. W.; Friend, R. H.; Greenham, N. C. Efficient Light-Emitting Diodes Based on Nanocrystalline Perovskite in a Dielectric Polymer Matrix. *Nano Lett.* **2015**, *15* (4), 2640−2644.

(23) Walzer, K.; Maennig, B.; Pfeiffer, M.; Leo, K. On Electrically Doped Transport Layers Highly Efficient Organic Devices Based on Electrically Doped Transport Layers. *Chem. Rev.* **2007**, *107* (4), 1233−1271.

(24) Pei, Q.; Yu, G.; Zhang, C.; Yang, Y.; Heeger, A. J. Polymer Light-Emitting Electrochemical Cells. *Science* **1995**, *269* (5227), 1086−1088.

(25) deMello, J. C.; Tessler, N.; Graham, S. C.; Friend, R. H.; C, J.; Tessler, N.; Graham, S. C.; Friend, R. H. Ionic Space-Charge Effects in Polymer Light-Emitting Diodes. *Phys. Rev. B: Condens. Matter Mater. Phys.* **1998**, *57* (20), 12951−12963.

(26) Slinker, J. D.; DeFranco, J. a; Jaquith, M. J.; Silveira, W. R.; Zhong, Y.; Moran-Mirabal, J. M.; Craighead, H. G.; Abruña, H. D.; Marohn, J. a; Malliaras, G. G. Direct Measurement of the Electric-Field Distribution in a Light-Emitting Electrochemical Cell. *Nat. Mater.* **2007**, *6* (11), 894−899.

(27) Van Reenen, S.; Matyba, P.; Dzwilewski, A.; Janssen, R. A. J.; Edman, L.; Kemerink, M. A Unifying Model for the Operation of Light-Emitting Electrochemical Cells. *J. Am. Chem. Soc.* **2010**, *132* (39), 13776−13781.

(28) Lenes, M.; Garcia-Belmonte, G.; Tordera, D.; Pertegás, A.; Bisquert, J.; Bolink, H. J. Operating Modes of Sandwiched Light-Emitting Electrochemical Cells. *Adv. Funct. Mater.* **2011**, *21* (9), 1581−1586.

(29) Meier, S. B.; Tordera, D.; Pertegás, A.; Roldán-Carmona, C.; Ortí, E.; Bolink, H. J. Light-Emitting Electrochemical Cells: Recent Progress and Future Prospects. *Mater. Today* **2014**, *17* (5), 217−223.

(30) Saidaminov, M. I.; Abdelhady, A. L.; Murali, B.; Alarousu, E.; Burlakov, V. M.; Peng, W.; Dursun, I.; Wang, L.; He, Y.; Maculan, G.; et al. High-Quality Bulk Hybrid Perovskite Single Crystals within Minutes by Inverse Temperature Crystallization. *Nat. Commun.* **2015**, *6* (May), 7586.

(31) Andričević, P.; Kollár, M.; Mettan, X.; Náfrádi, B.; Sienkiewicz, A.; Fejes, D.; Hernádi, K.; Forró, L.; Horváth, E. Three-Dimensionally Enlarged Photoelectrodes by a Protogenetic Inclusion of Vertically Aligned Carbon Nanotubes into CH$_3$NH$_3$PbBr$_3$ Single Crystals. *J. Phys. Chem. C* **2017**, *121* (25), 13549−13556.

(32) Bonard, J.; Salvetat, J.; Stöckli, T.; Forr, L. Field Emission from Carbon Nanotubes : Perspectives for Applications. *Appl. Phys. A: Mater. Sci. Process.* **1999**, *69* (3), 245−254.

(33) Fowler, R. H.; Nordheim, L. Electron Emission in Intense Electric Fields. *Proc. R. Soc. London, Ser. A* **1928**, *119* (781), 173−181.

(34) Yi, H. T.; Wu, X.; Zhu, X.; Podzorov, V. Intrinsic Charge Transport across Phase Transitions in Hybrid Organo-Inorganic Perovskites. *Adv. Mater.* **2016**, *28*, 6509−6514.

(35) Dong, H.; Wu, Z.; Xia, B.; Xi, J.; Yuan, F.; Ning, S.; Xiao, L.; Hou, X. Modified Deposition Process of Electron Transport Layer for Efficient Inverted Planar Perovskite Solar Cells. *Chem. Commun.* **2015**, *51* (43), 8986−8989.

(36) Shiraishi, M.; Ata, M. Work Function of Carbon Nanotubes. *Carbon* **2001**, *39* (12), 1913−1917.

(37) Bandiello, E.; Ávila, J.; Gil-Escrig, L.; Tekelenburg, E.; Sessolo, M.; Bolink, H. J. Influence of Mobile Ions on the Electroluminescence Characteristics of Methylammonium Lead Iodide Perovskite Diodes. *J. Mater. Chem. A* **2016**, *4* (47), 18614−18620.

(38) Eames, C.; Frost, J. M.; Barnes, P. R. F.; O'Regan, B. C.; Walsh, A.; Islam, M. S. Ionic Transport in Hybrid Lead Iodide Perovskite Solar Cells. *Nat. Commun.* **2015**, *6* (May), 7497.

(39) Almora, O.; Guerrero, A.; Garcia-Belmonte, G. Ionic Charging by Local Imbalance at Interfaces in Hybrid Lead Halide Perovskites. *Appl. Phys. Lett.* **2016**, *108* (4), 043903.

(40) Zhao, L.; Gao, J.; Lin, Y. L.; Yeh, Y.-W.; Lee, K. M.; Yao, N.; Loo, Y.-L.; Rand, B. P. Electrical Stress Influences the Efficiency of $CH_3NH_3PbI_3$ Perovskite Light Emitting Devices. *Adv. Mater.* **2017**, *29* (24), 1605317.

(41) Li, J.; Bade, S. G. R.; Shan, X.; Yu, Z. Single-Layer Light-Emitting Diodes Using Organometal Halide Perovskite/Poly-(Ethylene Oxide) Composite Thin Films. *Adv. Mater.* **2015**, *27* (35), 5196−5202.

(42) Wenger, B.; Nayak, P. K.; Wen, X.; Kesava, S. V.; Noel, N. K.; Snaith, H. J. Consolidation of the Optoelectronic Properties of $CH_3NH_3PbBr_3$ Perovskite Single Crystals. *Nat. Commun.* **2017**, *8* (1), 590.

(43) Puscher, B. M. D.; Aygüler, M. F.; Docampo, P.; Costa, R. D. Unveiling the Dynamic Processes in Hybrid Lead Bromide Perovskite Nanoparticle Thin Film Devices. *Adv. Energy Mater.* **2017**, *7* (15), 1−10.

(44) Zhang, H.; Lin, H.; Liang, C.; Liu, H.; Liang, J.; Zhao, Y.; Zhang, W.; Sun, M.; Xiao, W.; Li, H.; et al. Organic-Inorganic Perovskite Light-Emitting Electrochemical Cells with a Large Capacitance. *Adv. Funct. Mater.* **2015**, *25* (46), 7226−7232.

(45) Sharma, P.; Bhatti, T. S. A Review on Electrochemical Double-Layer Capacitors. *Energy Convers. Manage.* **2010**, *51* (12), 2901−2912.

(46) Fresta, E.; Costa, R. D. Beyond Traditional Light-Emitting Electrochemical Cells − a Review of New Device Designs and Emitters. *J. Mater. Chem. C* **2017**, *5* (23), 5643−5675.

(47) Aygüler, M. F.; Weber, M. D.; Puscher, B. M. D.; Medina, D. D.; Docampo, P.; Costa, R. D. Light-Emitting Electrochemical Cells Based on Hybrid Lead Halide Perovskite Nanoparticles. *J. Phys. Chem. C* **2015**, *119* (21), 12047.

(48) Bade, S. G. R.; Li, J.; Shan, X.; Ling, Y.; Tian, Y.; Dilbeck, T.; Besara, T.; Geske, T.; Gao, H.; Ma, B.; et al. Fully Printed Halide Perovskite Light-Emitting Diodes with Silver Nanowire Electrodes. *ACS Nano* **2016**, *10* (2), 1795−1801.

(49) Magrez, A.; Smajda, R.; Seo, J. W.; Horváth, E.; Ribič, P. R.; Andresen, J. C.; Acquaviva, D.; Olariu, A.; Laurenczy, G.; Forró, L. Striking Influence of the Catalyst Support and Its Acid-Base Properties: New Insight into the Growth Mechanism of Carbon Nanotubes. *ACS Nano* **2011**, *5* (5), 3428−3437.

(50) Szabó, A.; Andričević, P.; Pápa, Z.; Gyulavári, T.; Németh, K.; Horváth, E.; Forró, L.; Hernadi, K. Growth of CNT Forests on Titanium Based Layers, Detailed Study of Catalysts. *Front. Chem.* **2018**, *6*, 1−9.

Supporting Information: Light-Emitting Electrochemical Cells of Single Crystal Hybrid Halide Perovskite with Vertically Aligned Carbon Nanotubes Contacts

Pavao Andričević[1], Xavier Mettan[1], Márton Kollár[1], Bálint Náfrádi[1], Andrzej Sienkiewicz[1,2],

Tonko Garma[3], Lidia Rossi[1], László Forró*[1], Endre Horváth*[1]

1Laboratory of Physics of Complex Matter (LPMC), Ecole Polytechnique Fédérale de Lausanne, Centre Est, Station 3, CH-1015 Lausanne, Switzerland;

2ADSresonances SARL, Route de Genève 60B, CH-1028 Préverenges, Switzerland;

3Power Engineering Department, Faculty of Electrical Engineering, Mechanical Engineering and Naval Architecture, University of Split, Split, Croatia
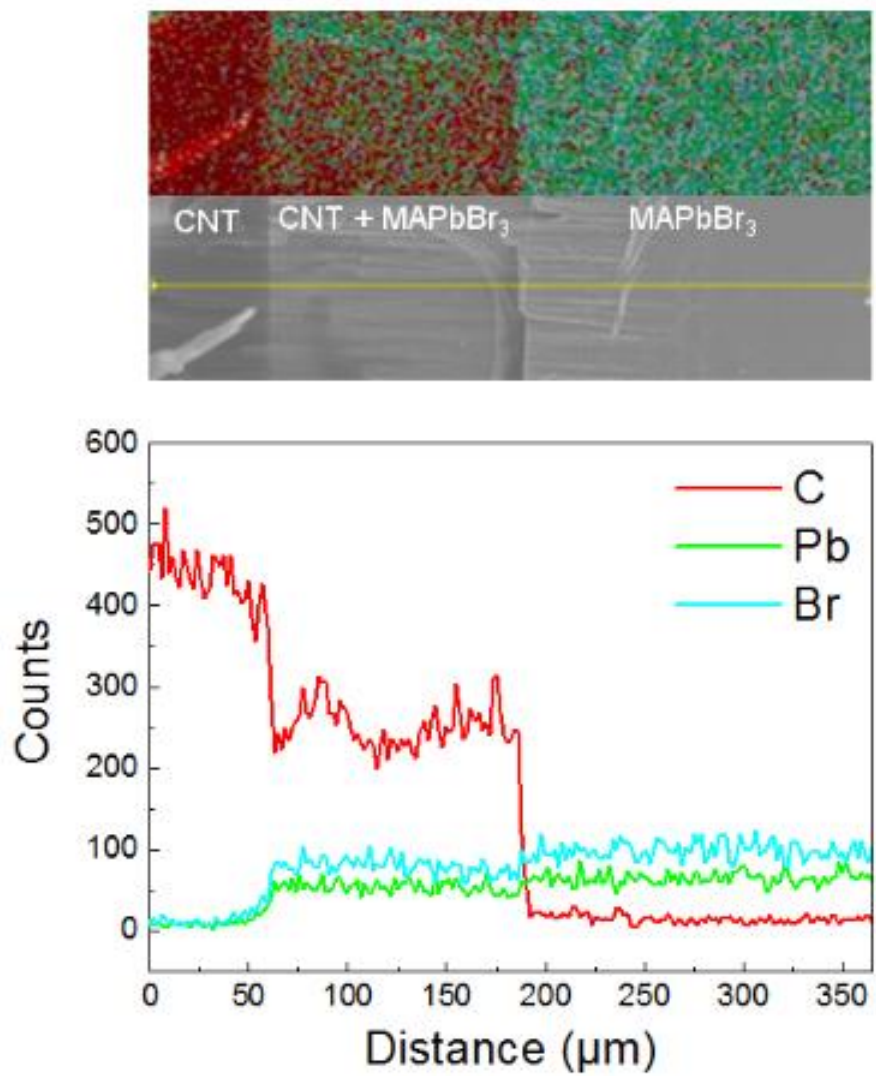
Figure S1. Elemental analysis by EDX of the VACNT/MAPbBr$_3$ interface showing clearly the engulfed, overlapping region between the CNTs and the perovskite SC.
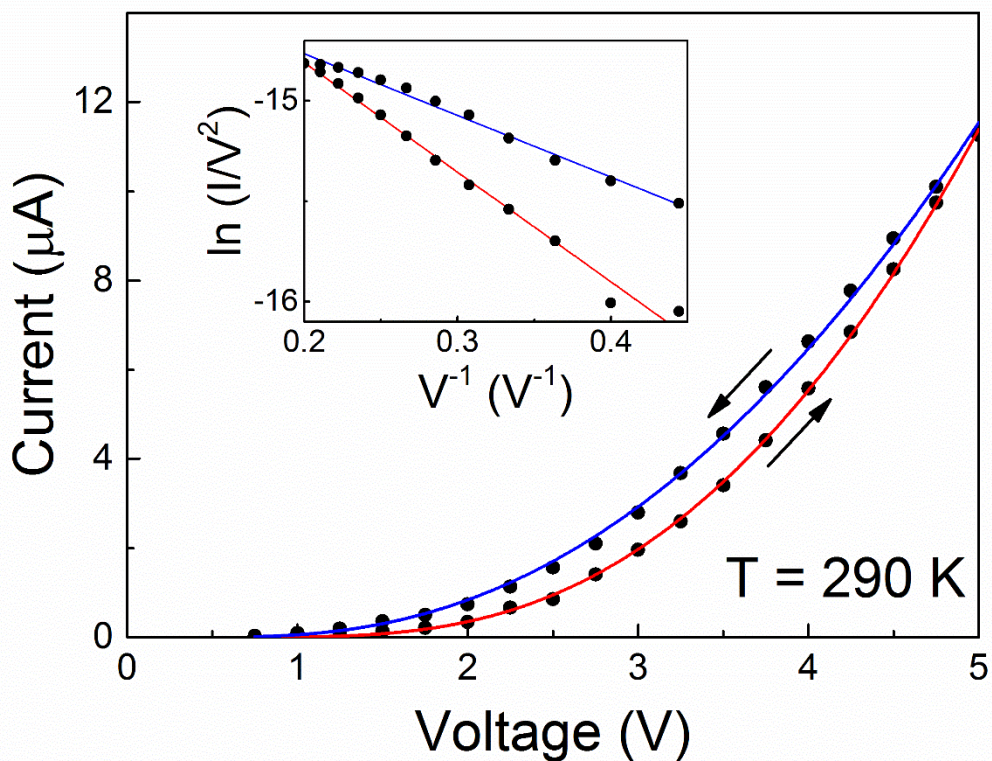
Figure S2. The I-V characteristics of MAPbBr$_3$ with two CNTs electrodes (symmetric device) at 290 K. The inset shows the Fowler-Nordheim plot of the I-V characteristics, where the linear dependence of ln(I/V^2) in $1/V$ supports efficient charge injection from the CNTs by field emission.
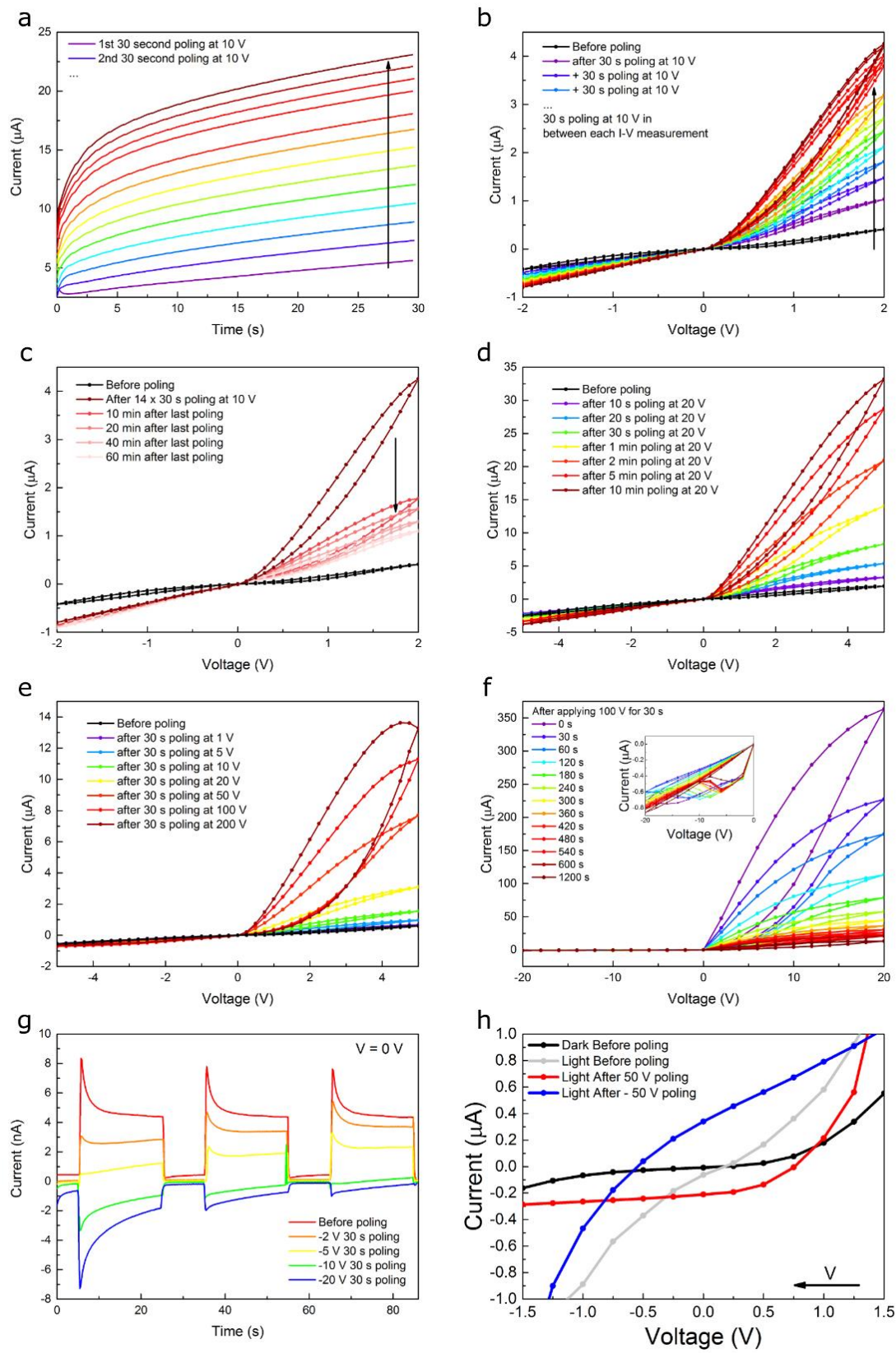
Figure S3. (a) The time evolution of the current during the poling treatment of the VACNT/MAPbBr$_3$ symmetric device at the bias voltage of +10 V observed for 13 consecutive poling cycles. (b) Change of the device I-V characteristics after multiple poling intervals. (c) Tracking the change of I-V characteristics of the poled device as a function of time. (d) Dependence of the I-V characteristic changes as a function of time of poling and (e) poling voltage. (f) Tracking the change of I-V characteristics of a poled device at 100 V for 30 s in time. (g) On-off measurements showing the switchable photovoltaic effect when poled with the bias voltage of the opposite polarity. (h) Switchable photovoltaic and memristive effect visible on I-V curves measured immediately after poling by opposite voltage polarities.

To understand more in detail the effect of poling on our samples we applied different poling schemes (time, voltage, polarity) followed by quick voltage scans (2 V s^{-1}) to study the change in the I-V characteristics. By applying a 10 V bias voltage the devices increases its current in 30 seconds from 3 µA to 5 µA, by repeating these 30 seconds interval for 12 times with quick I-V sweeps in between the current through the device reached 23 µA (Figure S3a), increasing the forward bias current and diode quality as seen in Figure S3b. Unfortunately, this improved diode characteristics are not long lasting. They return to their initial values after 1 hour as seen in Figure S3c. The dependence on different poling times (10 seconds to 10 minutes) and poling voltages (1 V to 200 V) were also studied as shown on Figure S3d and S3e, respectively. As expected the higher the poling time or voltage the bigger increase in current was measured. However, again when measuring quick I-V scans after a 30 seconds preconditioning with a high bias voltage of 100 V it is visible that even after 30 second the increased current (at 20 V) drops from 363 to 228 µA (Figure S3f). Continuing to decrease to 44 µA after 300 seconds and to only 14 µA after 1200 seconds. As the device exhibited photovoltaic activity detecting light at 0 V, preconditioning with

bias voltages of negative polarities (reverse bias) were applied to suppress the open circuit currents. Interestingly, with sufficiently high voltages it is possible to switch the photovoltaic effect achieving negative open circuit currents (Figure S3g). This switchable photovoltaic and memristive effect is also visible directly on the I-V curves of Figure S3h done immediately after the poling. All measurements were performed under visible light illumination (intensity 1.02 mWcm^{-2}) at room temperature and ambient conditions.
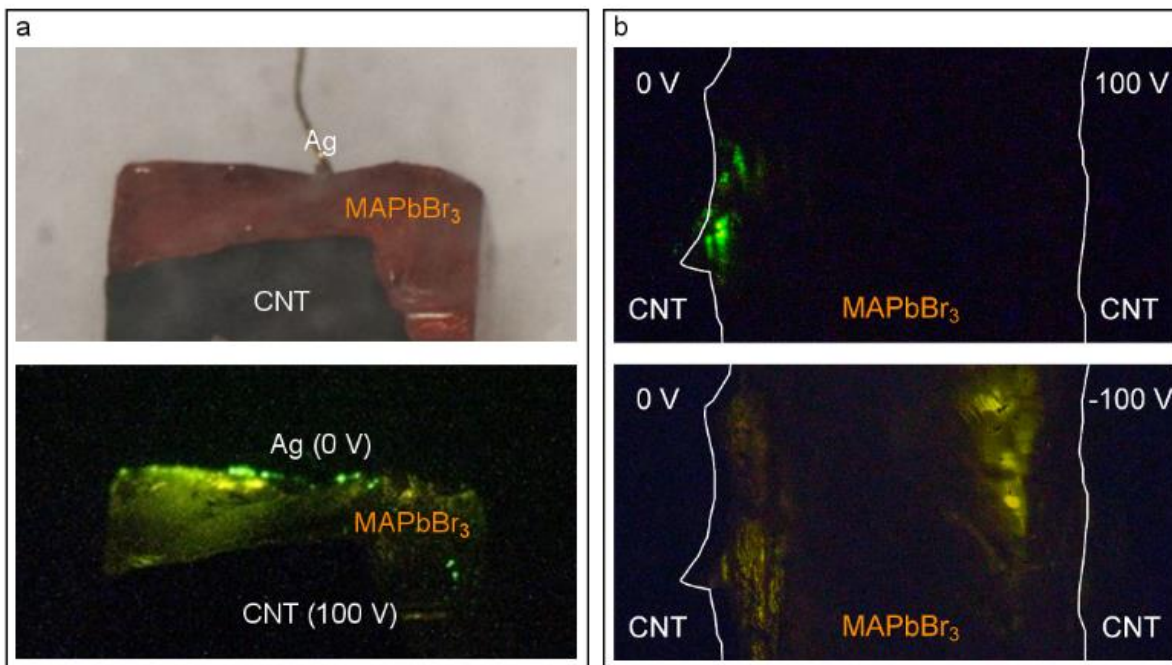

Figure S4. Images of the VACNT/MAPbBr$_3$ (a) asymmetric and (b) symmetric device acquired at room temperature. The spots of carrier recombination emitting most of the bright green light are located close to the electrode with the lower voltage.

In order to examine the durability of the device and to eliminate the possibility that the quenching of the device is due to the passing of time and not the change in temperature, measurements of light intensity were done at 25 K every 5 minutes for an hour. (Figure S4e and S4f) They showed that during an hour both the normalized intensity and current fell only to 90% of its initial value, eliminating the possibility that this had a significant influence to our prior measurements. However, pointing out that the perovskite light emitting material loses its intensity in time, and is something that should be studied more in detail.
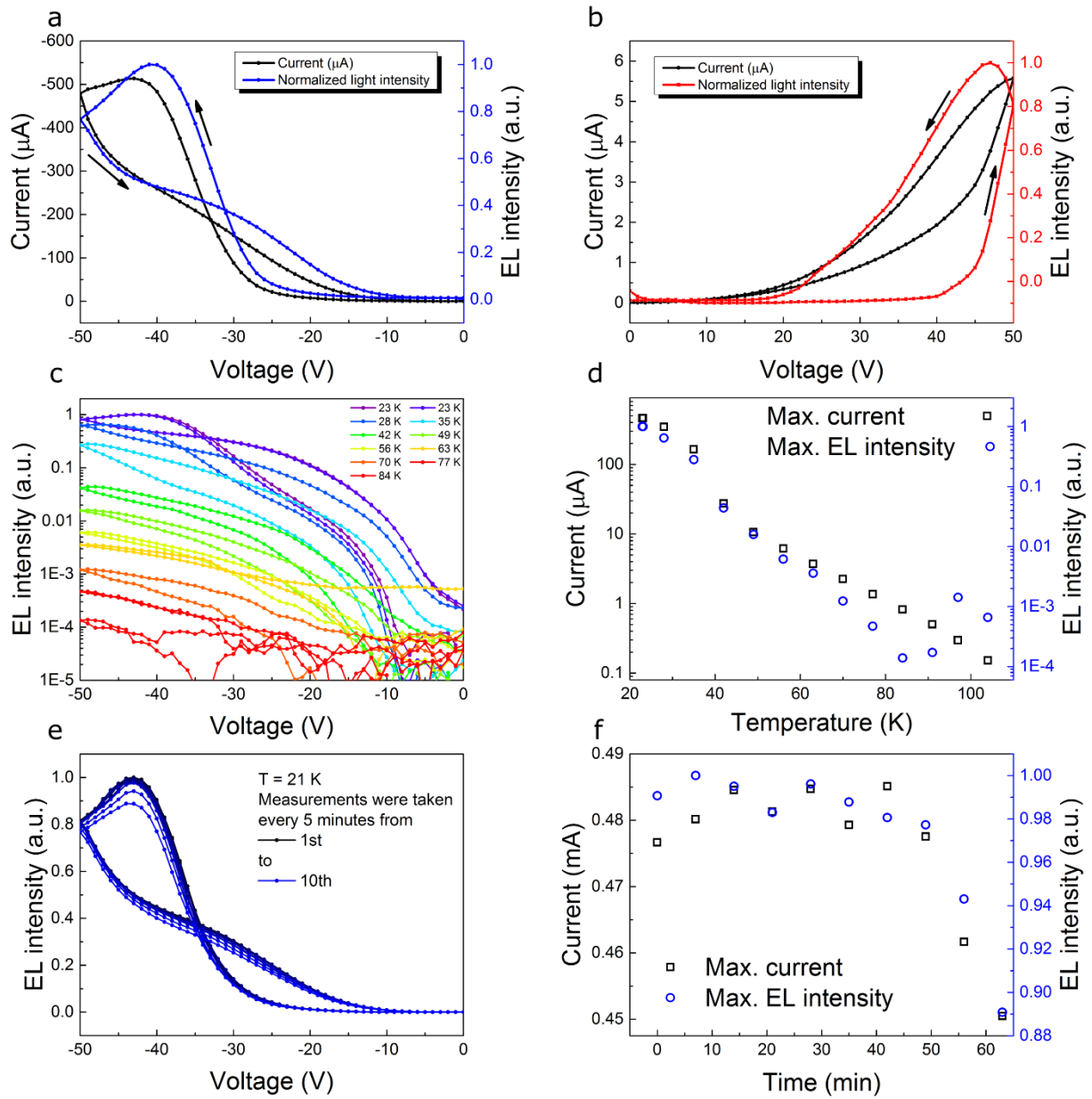
Figure S5. Dependence of the current through the device and normalized intensity of light emission with (a) negative and (b) positive bias voltages at 25 K. (voltage sweep speed 0.45 V/s) (c-d) Temperature dependence of normalized EL intensities of the light emission and current through the device for negative bias voltages. (e-f) Time dependence of normalized EL intensities of the light emission and current through the device for negative bias voltages. Measurements were done every 5 minutes for 1 hour.
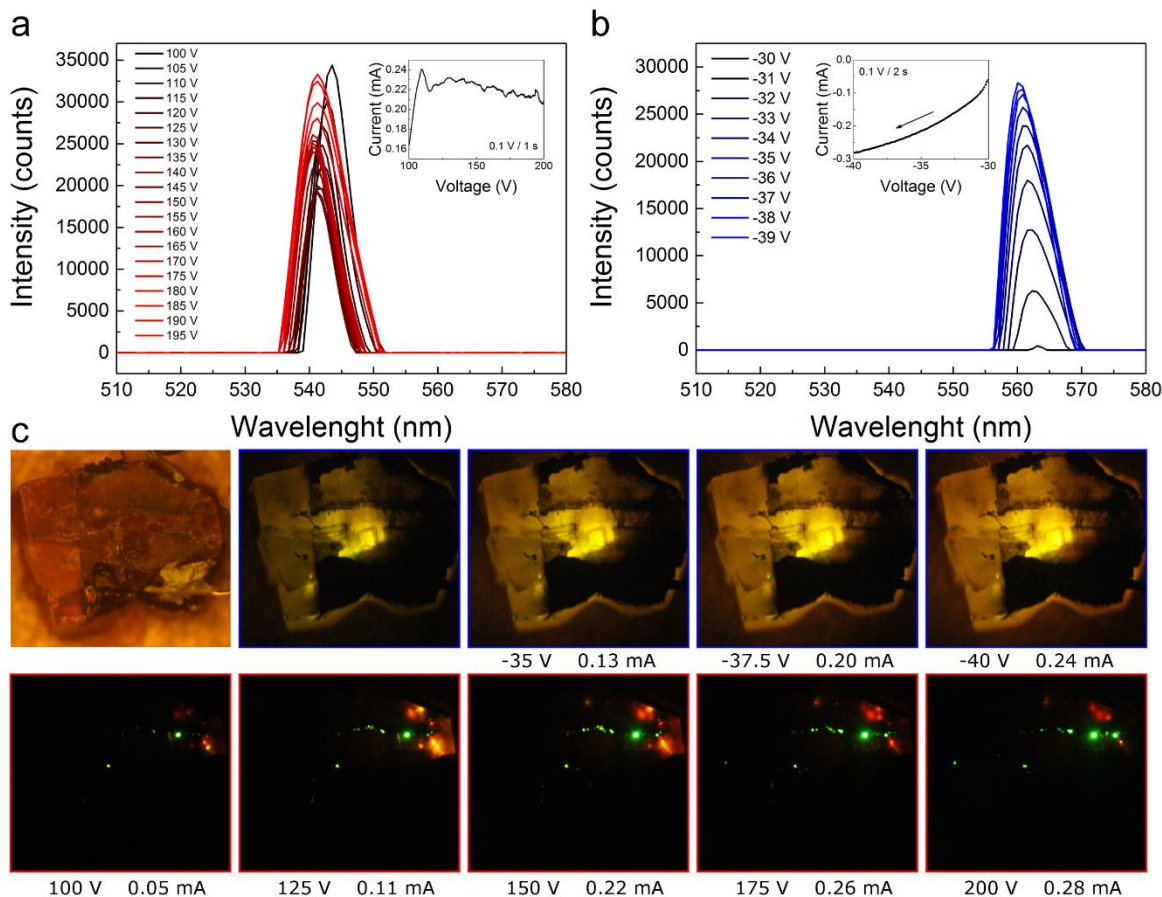
Figure S6. The EL spectra collected at 23 K in vacuum as a function of the bias voltage for positive (a) and negative (b) bias polarities. Inset: The I-V characteristics measured during acquiring spectra. (c) Images of the device and light emission inside a vacuum chamber at 23 K as a function of the applied bias voltage. The intensities of the resulting current across the device are also indicated.

Table S1. Peak center (X_c) and full width at half maximum (FWHM) obtained from Gaussian fit of the EL spectra in Figure S5.

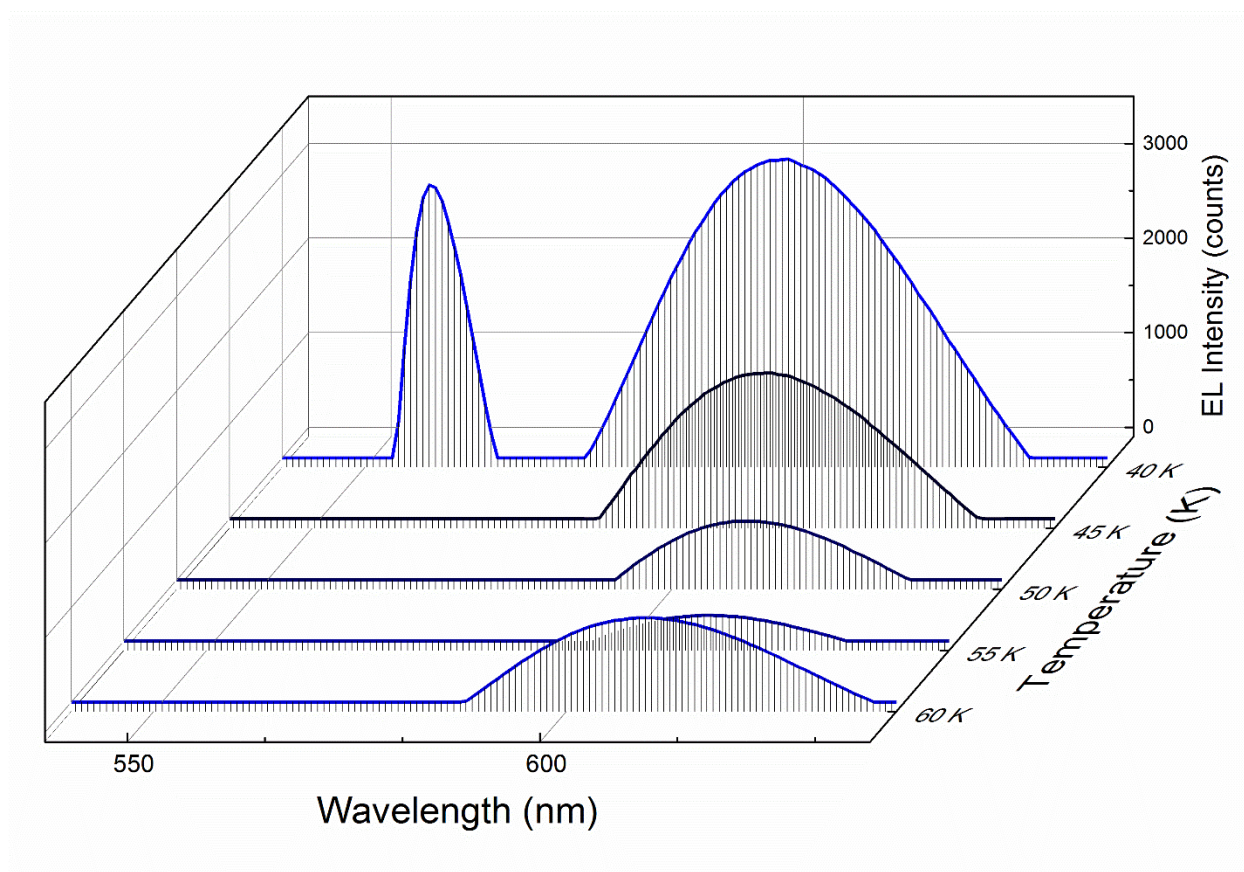| Voltage range (V)	X_c (nm)	FWHM (nm)
100 to 195	541.9 ± 0.7	6 ± 1
-30 to -40 (Figure S5)	562.3 ± 0.7	6.9 ± 0.2
-30 to -40 (All obtained spectra)	562.2 ± 0.6	7.4 ± 0.7

Figure S7. EL spectra collected in the temperature range 40-60 K showing the disappearance of the peak at 562 nm and temperature dependence of the peak at 590 nm. Important to point out is the change in bias voltage from -40 V (40, 45 and 50 K) to -50 V at 55 K and -100 V at 60 K to be able to acquire the spectra.
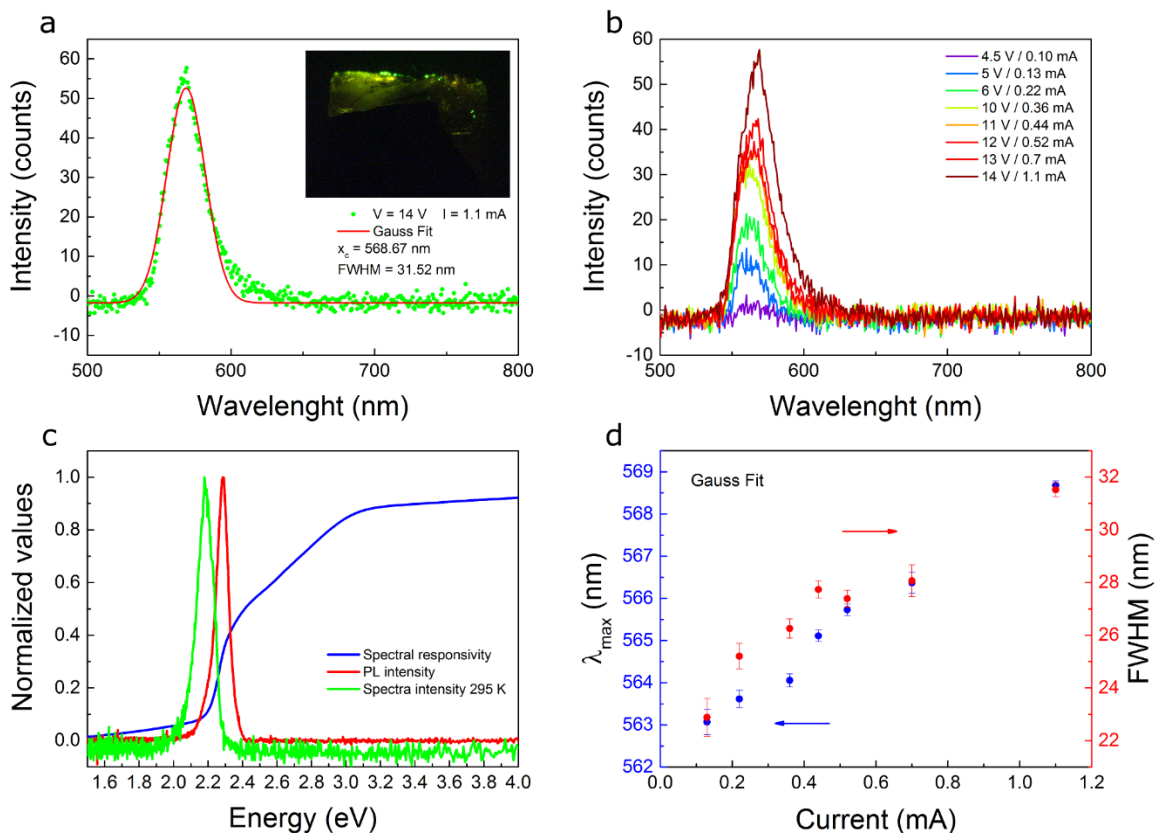
Figure S8. The EL spectra recorded for the VACNT/MAPbBr$_3$ asymmetric device acquired at room temperature. (a) The typical EL spectrum fitted with a Gaussian function (red solid line). Inset: Image of light emission at room temperature. (b) The EL spectra acquired at different bias voltages. (c) The spectral responsivity of the MAPbBr$_3$ crystal (blue trace), the photoluminescence (PL) spectra under excitation at λ_{exc} = 470 nm (red trace) and the EL spectra (green trace). (d) The dependence of the peak wavelength, λ_{max}, and full width at half maximum (FWHM) of the Gaussian fits of EL spectra as a function of the current through the device.

When decreasing temperature, the spectra peak moves to lower wavelengths, simultaneously getting narrower. (Figure S9d) The shift to lower wavelengths can be credited to the temperature dependence of the energy bandgap of semiconductors. With the decrease of thermal energy, the interatomic spacing increases, increasing the potential seen by the electrons in the material,

consequently rising the size of the energy bandgap. Interestingly, around the temperature of the phase transition of MAPbBr$_3$ 148 K, a second peak appears giving a shoulder on the spectra toward lower wavelengths (Figure S9c). The same peak disappears just after the phase transition not changing drastically the trend of the main peak.
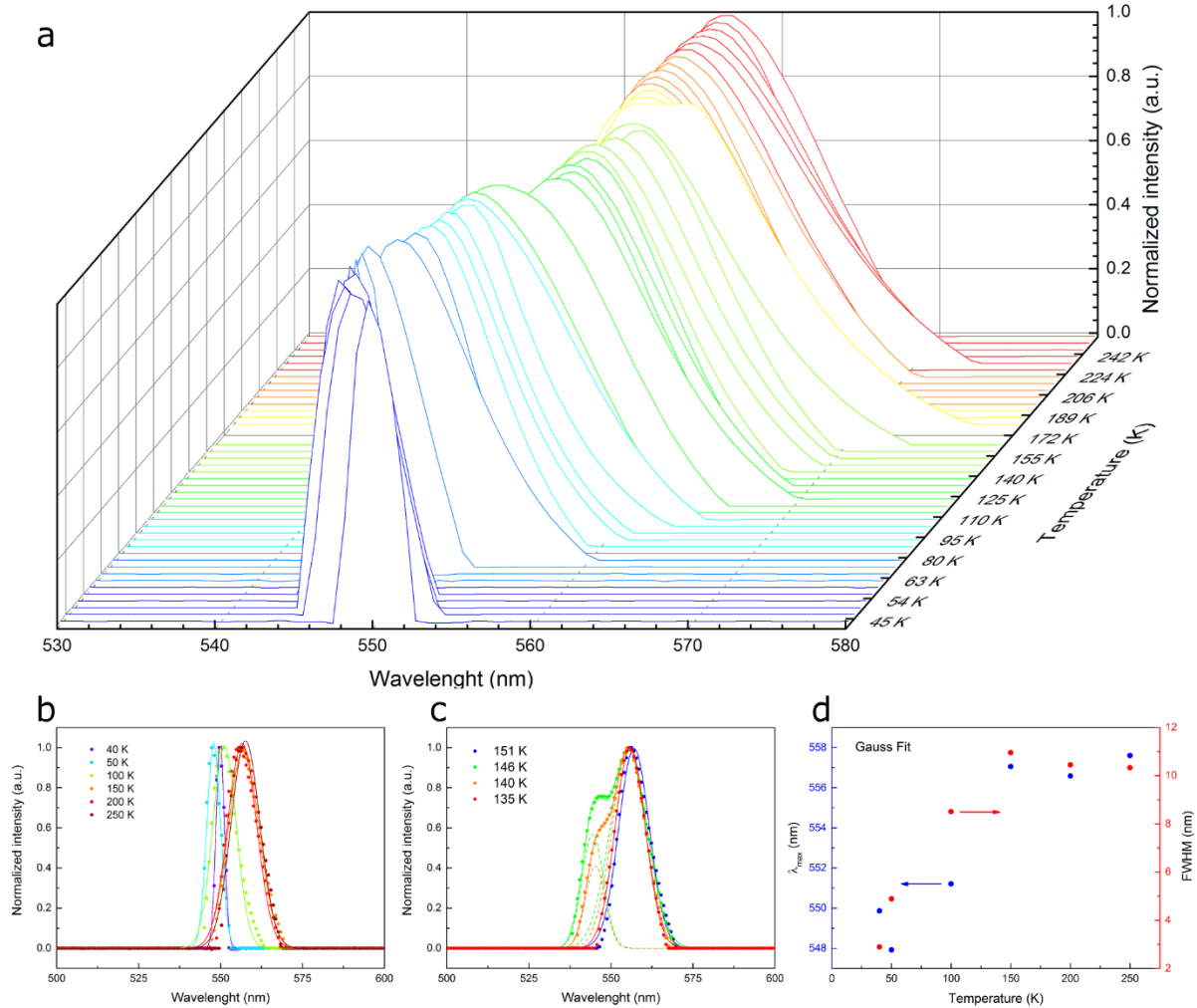

Figure S9. (a) The normalized EL spectra of the VACNT/MAPbBr$_3$ asymmetric device collected in the temperature range 40 – 250 K. (a) The EL spectra fitted with a Gaussian function every 50 K and (c) around the phase transition of MAPbBr$_3$ (d) The temperature dependence of the peak wavelength, λ_{max}, and full width at half maximum (FWHM) of the Gaussian fits of the acquired EL spectra.

A constant voltage poling scheme was applied to the VACNT/MAPbBr$_3$ sample to study the response of the ions inside the perovskite single crystal. Since the ions feature different diffusion activation energies, as stated by Puscher et al.,[1] also the differences in their motion rates, which are independent of the poling scheme, can be expected. A 10 hours' time-dependent response of the current upon applying a constant external voltage of 10 V is shown in Figure S10. A constant increase of current is visible, which fits to a tri-exponential function:

$$y = y_0 + A_1 e^{\frac{-(x-x_0)}{t_1}} + A_2 e^{\frac{-(x-x_0)}{t_2}} + A_3 e^{\frac{-(x-x_0)}{t_3}}$$

This is a typical feature of LECs and can be attributed to the slow enhancement in charge injection processes due to the formation of the EDLs at the electrode interface and the sub- sequent growth of the doped regions. Time constants t_1, t_2, t_3 were calculated and are 63.6±0.4 s, 35.23±0.02 min, 7.482±0.007 h respectively. The shortest of the three processes is the fast formation of electric double layers (EDLs) by halide drift due to the lowest diffusion activation energy. This is in good agreement with other studies, where the effect of the diffusion of the halides was observed within a few seconds.[1] Given that MA+ cations have higher diffusion activation energies than halides, the second time constant is presumably caused by their alignment and migration toward the electrode interface. The third and slowest process is attributed to the growth of the charge carrier doped layers as it has been observed in LECs.[1]
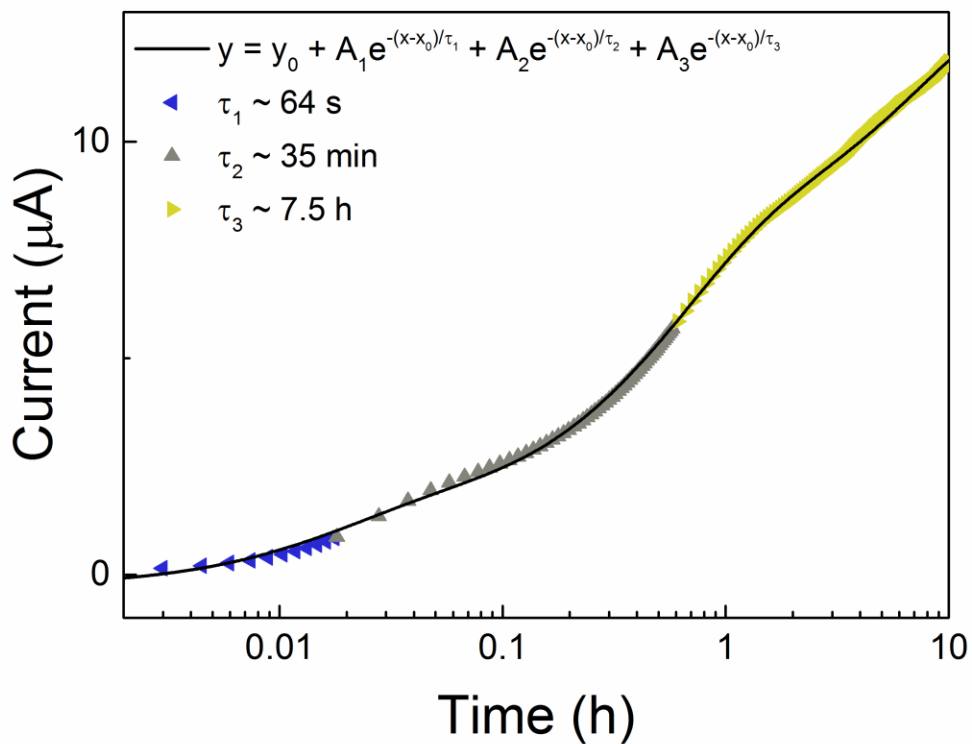
Figure S10. The time evolution of the current during the poling treatment of the VACNT/MAPbBr$_3$ symmetric device at the bias voltage of 10 V. The color code represents the three formation processes. The electric double layer formation by halide drift (blue), imbalance in the electrode potentials and/or organic cation diffusion (gray) and the growth of charge carrier doped layers (yellow). The tri-exponential fitting is given as the solid black line.

A certain bias (e.g., 2 V) was applied to the VACNT/MAPbBr$_3$/VACNT device (thickness 1 mm, surface area 10 mm^2) for a short period of time ($\approx$ 15 s) in the dark to accumulate the ions at the perovskite/CNT interfaces. In other words, to charge the C$_i$ of the device, which represents the capacitance from the blocking of ions at the electrode interfaces. The device was then rapidly switched to zero bias to measure the discharge current (Figure S11a, inset). The accumulated charge density at the bias (2 V) is the time integral of the discharge current. Figure S11a shows the measured charge densities of the accumulated ions at the interfaces under various biases. The slope of the curve indicates a C$_i$ value of $\approx$ 1 μF cm^{-2}. This large areal capacitance exceeds that of conventional electrostatic capacitors with a typical value of 0.1 μF cm^{-2}. The results suggest a potential application as solid-state supercapacitors by using the organic–inorganic perovskites. Furthermore, the dependence of the areal capacitance to the time of poling was measured. In Figure S11b we can clearly see an increase in capacitance with poling time.
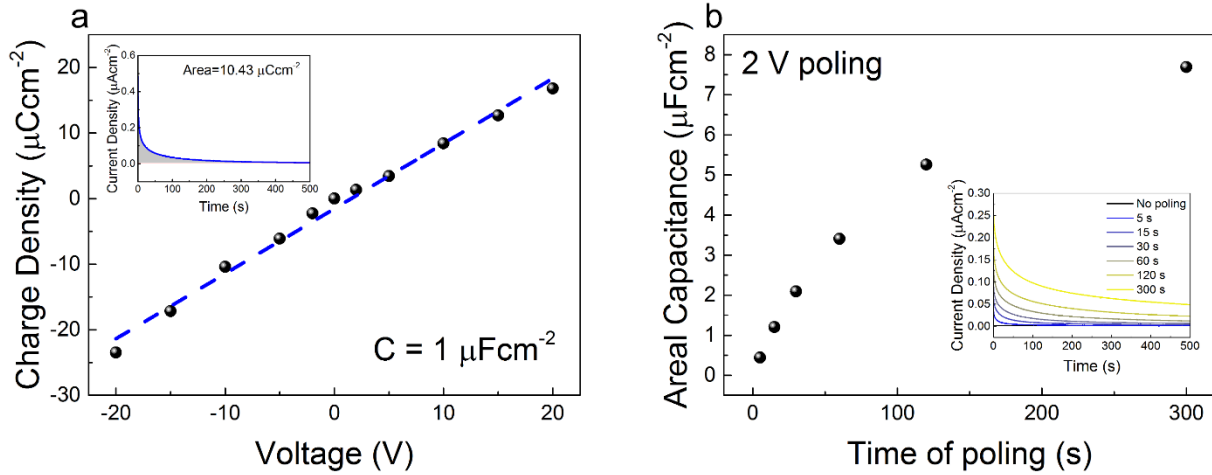

Figure S11. (a) Interface charge densities of the VACNT/MAPbBr$_3$/VACNT device at different bias voltages. Inset: Discharge process in time after charging the device for 15 s with 10 V. (b) Areal capacitance of the device for different time of poling at 2 V. Inset: Discharge process dynamics for different time of poling.
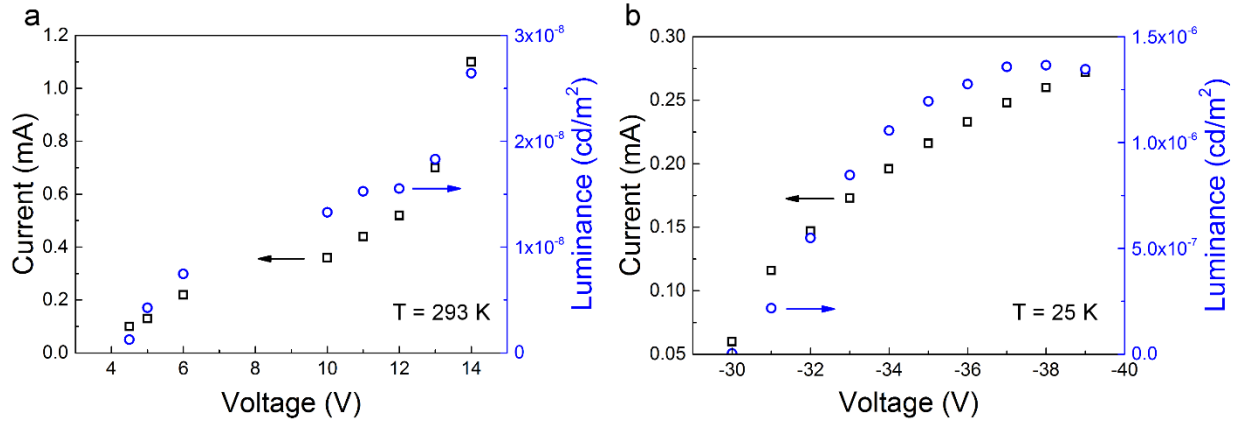
Figure S12. Luminance-current versus voltage at (a) room and (b) cryogenic temperatures from EL spectra of the VACNT/MAPbBr$_3$ (a) asymmetric and (b) symmetric device.

Luminance of the light emission was calculated by:

$$L = \frac{d\Phi_v}{dS d\Omega \cos\theta} \qquad (1)$$

Where dS is the emission area [m^2], $d\Omega$ the infinitesimal solid angle [sr] containing the direction, θ the angle to the detector and $d\Phi_v$ the luminous flux [lm]:

$$d\Phi_v = \frac{A \times s}{t_{int}} \times V(\lambda) \qquad (2)$$

Where A is the area under the EL spectra, $s = 5.3 \times 10^{-18}$ J/counts the sensitivity of the spectrometer at 555 nm, t_{int} the integration time and $V(\lambda) = 683$ lm/W the photopic spectral luminous efficiency at 555 nm. A half sphere emission was taken as the sample was laid down on a surface.

The luminance at room temperature, in Figure 3a and b, is calculated using $d\Phi_v = P_{detected} \times V(\lambda)$ with equations (1).

However, at low temperatures the intensity power was not measured directly. Only the dependence of the intensity with current and voltage was obtained. To calculate these values, the

difference in EL intensity (spectrometer) at room and low temperature and the intensities of light flashes at room temperature (Thorlabs PM100D photodetector) were used as follows:

$$P_{25K} = P_{293K} \times \frac{L_{25K}(spectrometer)}{L_{293K}(spectrometer)} \qquad (3)$$

At 0.23 mA of current an average light intensity of 1 nW was measured at room temperature which will then correspond to 360 nW at 25 K. Finally, from the intensity-current dependence we can calculate the LIV curve at cryogenic temperatures.

At room temperature, an average emission area of 250 μm^2 is used as the light emission is produced in flashes, whereas at low temperatures a 2.25 mm^2 emission surface is taken.
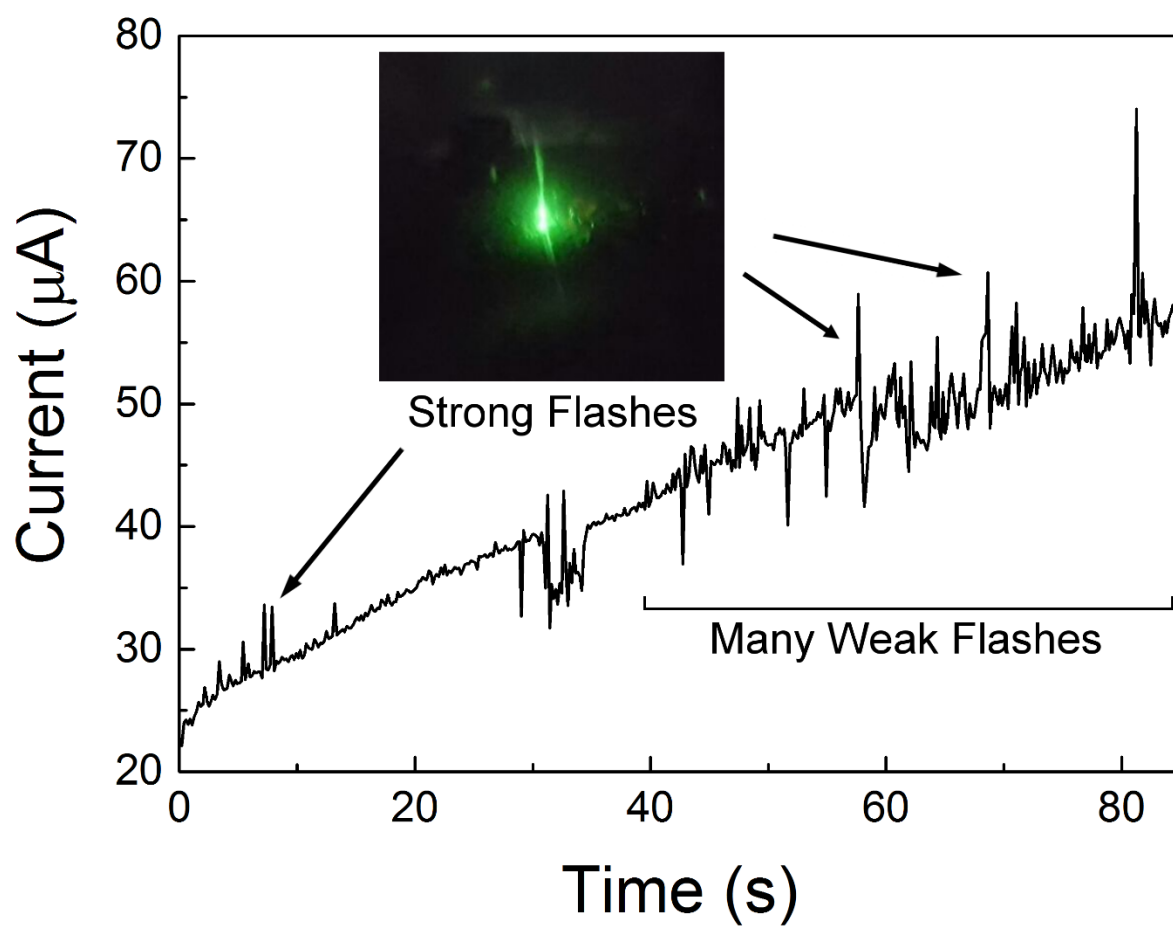
Figure S13. The time evolution of current during the poling treatment of the VACNT/MAPbBr$_3$ device at 30 V and room temperature. Bright green flashes of emitted light correspond in time with the sudden peaks in current.

Table S2. Comparative table of the performances of the best-in-class perovskite based LECs and LEDs.

Device structure	Single compound or Composite	Selective electrodes	Polycrystalline or Single Crystal	Light emitting mechanism	Turn-on Voltage (V)	Layer thickness (μm)	Turn-on Electric field (V/m)	Luminescence Max (cd/m²)	Reference
ITO / PEDOT:PSS / PK NP:TMPE:LiCF$_3$SO$_3$ / Al	Composite	No	Polycrystalline	LEC	11	0.1	1.1×10^8	1.3	Aygüler et al. [2]
ITO / PEDOT:PSS / PK NP / Al	Single compound	No	Polycrystalline	LEC	-	0.06	-	-	Aygüler et al. [2]
ITO / Pero-PEO composite / In (Ga,Au)	Composite	No	Polycrystalline	LEC	3	≈0.2	≈1.5×10^7	4064	Li et al. [3]
ITO / PEDOT:PSS / Perovskite / MoO$_3$ / Au	Single compound	Yes	Polycrystalline	LEC	2.4	0.4	6×10^6	-	Zhang et al. [4]
ITO / Pero-PEO composite / Ag NW	Composite	No	Polycrystalline	LED/LEC	2.6	3	8.7×10^5	21014	Bade et al. [5]
Polymer substrate / SWCNT / Pero-PEO composite / Ag NW	Composite	≈No	Polycrystalline	LED/LEC	2.6	3	8.7×10^5	360	Bade et al. [5]
ITO / TiO$_2$ / Perovskite / F8 / MoO$_3$ / Au	Single compound	Yes	Polycrystalline	LED	3.3	0.02	1.7×10^8	364	Tan et al. [6]
Glass / SOCP / MAPbBr$_3$ / TPBI / LiF / Al	Single compound	Yes	Polycrystalline	LED	≈3	≈0.4	≈7.5×10^6	≈15000	Cho et al. [7]
ITO / PEDOT:PSS / MAPbBr$_3$ / SPB-02T / LiF / Ag	Single compound	Yes	Polycrystalline	LED	≈2	0.4	≈5×10^6	3490	Yu et al. [8]
VACNT / SC MAPbBr$_3$ / VACNT	Single compound	No	Single Crystal	LEC	≈26 (23K)	≈2000	≈1.3×10^4	1000 (0.5 mA)	This work
					≈100 (293K)		≈5×10^4	Avg. 60 (50 μA) Max. 1800 (2.8 mA)	

REFERENCES

[1]   B. M. D. Puscher, M. F. Aygüler, P. Docampo, R. D. Costa, *Adv. Energy Mater.* **2017**, *7*, 1.

[2]   M. F. Aygüler, M. D. Weber, B. M. D. Puscher, D. D. Medina, P. Docampo, R. D. Costa, *J. Phys. Chem. C* **2015**, *119*, 150415033719003.

[3]   J. Li, S. G. R. Bade, X. Shan, Z. Yu, *Adv. Mater.* **2015**, *27*, 5196.

[4]   H. Zhang, H. Lin, C. Liang, H. Liu, J. Liang, Y. Zhao, W. Zhang, M. Sun, W. Xiao, H. Li, S. Polizzi, D. Li, F. Zhang, Z. He, W. C. H. Choy, *Adv. Funct. Mater.* **2015**, *25*, 7226.

[5]   S. G. R. Bade, J. Li, X. Shan, Y. Ling, Y. Tian, T. Dilbeck, T. Besara, T. Geske, H. Gao, B. Ma, K. Hanson, T. Siegrist, C. Xu, Z. Yu, *ACS Nano* **2016**, *10*, 1795.

[6]   Z.-K. Tan, R. S. Moghaddam, M. L. Lai, P. Docampo, R. Higler, F. Deschler, M. Price, A. Sadhanala, L. M. Pazos, D. Credgington, F. Hanusch, T. Bein, H. J. Snaith, R. H. Friend, *Nat. Nanotechnol.* **2014**, *9*, 1.

[7]   A. H. Cho, S. Jeong, M. Park, Y. Kim, S. H. Im, R. H. Friend, T. Lee, **2014**, *350*, 1222.

[8]   J. C. Yu, D. Bin Kim, E. D. Jung, B. R. Lee, M. H. Song, *Nanoscale* **2016**, *8*, 7036.